Atmos. Chem. Phys. Discuss., https://doi.org/10.5194/acp-2018-643
Manuscript under review for journal Atmos. Chem. Phys.
Discussion started: 23 July 2018

Atmospheric Chemistry and Physics Discussions

Top–down estimates of black carbon emissions at high latitudes using an atmospheric transport model and a Bayesian inversion framework

Nikolaos Evangeliou *, Rona L. Thompson, Sabine Eckhardt, Andreas Stohl

Norwegian Institute for Air Research (NILU), Department of Atmospheric and Climate Research (ATMOS), Kjeller, Norway.

* Correspondence to: N. Evangeliou (nikolaos.evangeliou@nilu.no)

Atmos. Chem. Phys. Discuss., https://doi.org/10.5194/acp-2018-643
Manuscript under review for journal Atmos. Chem. Phys.
Discussion started: 23 July 2018

Atmospheric Chemistry and Physics Discussions

Abstract

This paper presents the results of BC inversions at high northern latitudes (>50°N) for the 2013–2015 period. A sensitivity analysis was performed to select the best representative species for BC and the best prior emission dataset. The same model ensemble was used to assess the uncertainty of the posterior emissions of BC due to scavenging and removal and due to the use of different prior emission inventory. The optimised emissions of BC were high close to the gas flaring regions in Russia and in Western Canada (Alberta), where numerous power and oil/gas production industries operate. The annual posterior emissions of BC at latitudes above 50°N were estimated as 560±171 kt yr^{-1}, significantly smaller than in ECLIPSEv5 (745 kt yr^{-1}), which was used and the prior information in the inversions of BC. The average relative uncertainty of the inversions was estimated to be 30%.

Posterior concentrations of BC simulated over Arctic regions were compared with independent observations from flight and ship campaigns showing, in all cases, smaller bias, which in turn witnesses the success of the inversion. Posterior emissions of BC in North America are driven by anthropogenic sources, while biomass burning appeared to be less significant as it is also confirmed by satellite products. In North Europe, posterior emissions were estimated to be half compared to the prior ones, with the highest releases to be in megacities and due to biomass burning in Eastern Europe. The largest emissions of BC in Siberia were calculated along the transect between Yekaterinsburg and Chelyabinsk. Flaring emissions in Nenets-Komi oblast (Russia) were estimated to be much lower than in the prior emissions, while in Khanty-Mansiysk (Russia) they remained the same after the inversions of BC. Increased emissions in the borders between Russia and Mongolia are probably due to biomass burning in villages along the Trans-Siberian Railway.

Atmos. Chem. Phys. Discuss., https://doi.org/10.5194/acp-2018-643
Manuscript under review for journal Atmos. Chem. Phys.
Discussion started: 23 July 2018

1 Introduction

Light absorbing components, such as black carbon (BC), is the main of atmospheric particulate matter, affecting air quality, weather and climate. BC originates from the incomplete combustion of fossil fuels (primarily coal and diesel) as well as from the burning of biomass and biofuels. BC particles affect cloud formation and precipitation as they act as cloud condensation nuclei in their hydrophilic form (Wang et al., 2016). BC is also a major driver of climate change contributing to global warming with a radiative forcing at the top of the atmosphere ranging between 0.17 and 0.71 W m^{-2} (Bond et al., 2013; Myhre et al., 2013; Wang et al., 2014). BC deposited in Arctic snow surfaces in concentrations of up to 30 ng g^{-1} can reduce snow albedo by 1–3% (Hegg et al., 2009) in fresh snow and up to 3 times more as snow ages and the BC particles become more concentrated (Clarke and Noone, 1985). Airborne BC also warms the air and reduces tropical cloudiness by absorbing the incoming solar radiation (Ackerman, 2000). It also reduces atmospheric visibility and increases aerosol optical depth (Jinhuan and Liquan, 2000). From a health perspective, BC particles, generally being sub-micron in size, can penetrate into the lungs and cause pulmonary diseases (e.g., Wang et al., 2014).

To improve understanding about how BC affects climate and to develop effective policies to tackle BC's associated environmental problems requires accurate knowledge of the emissions and their spatiotemporal distribution. Most commonly, BC emission inventory datasets are built by "bottom up" approaches, which are based on activity data and emission factors and proxy information for spatial disaggregation, but these methods are considered to have large uncertainties (Cao et al., 2006). Numerous global or regional emission inventories of BC have been constructed previously (Bond et al., 2004; Schaap et al., 2004; Streets et al., 2003); nevertheless, emission uncertainties contribute significantly to the overall uncertainty of modelled concentrations of BC. Emission uncertainties affect even more significantly regional/episodic simulations, as in many cases emissions deviate from the annual mean. Such studies represent a useful tool to improve our understanding of the relationship between observed concentrations of BC and BC emissions. Furthermore, BC emissions have their most pronounced effect on the regional scale due to the relatively short atmospheric lifetime of BC (Hodnebrog et al., 2014; Samset et al., 2014),.

The relative differences between different emission inventories are largest for the high latitudes (AMAP, 2015) and particularly in high-latitude Russia where emission information is poor. For this area, a new satellite-based high-resolution inventory showed that BC emissions from Biomass Burning (BB) might have been 3.5 times higher than emissions

given in the Global Fire Emissions Database (GFEDv4) (Hao et al., 2016), if more realistic emission factors are used (May et al., 2014). Furthermore, new sources of BC in the same area have been identified recently. For example, emissions from gas flaring by the oil industry have been missing from most emission inventories and may be an important source of BC at high latitudes (Stohl et al., 2013). For instance, in 2008 Russia was responsible for nearly one third of the gas flared globally (Elvidge et al., 2009). However, the gas flaring source is highly uncertain. For example, based on isotopic measurements, Winiger et al. (2017) reported recently that the contribution from gas flaring to BC measured at Tiksi in Siberia is lower than estimated by Stohl et al. (2013), while recently published bottom-up inventories (Huang et al., 2015; Huang and Fu, 2016) suggested even higher gas flaring emissions. Finally, Popovicheva et al. (2017) reported that one existing emission dataset of BC captured surface concentrations in the Russian Arctic quite efficiently.

In this study, we estimated the BC emissions at high northern latitudes using atmospheric observations of BC in a Bayesian inversion framework. Emissions were estimated for the region north of 50°N because this is the region with the largest influence on Arctic surface concentrations (Klonecki, 2003; Stohl, 2006). We determine the emissions with monthly time resolution for the years 2013, 2014 and 2015. We first describe the observation data, the transport model and the Bayesian inversion technique used, as well as the prior emission information. We then assess the sensitivity of the transport model to different scavenging coefficients (below-cloud and in-cloud) for BC and to different emission inventories. We finally present optimised BC emissions, discuss these results in comparison with independent estimates and calculate the uncertainty of the inversions with respect to different scavenging parameters used for BC and using four different prior emission datasets.

2 Methodology

2.1 Observation network

Atmospheric observations of BC were retrieved from the World Data Centre for Aerosols (http://ebas.nilu.no) and from the International Arctic Systems For Observing The Atmosphere (http://www.esrl.noaa.gov/psd/iasoa/). An overview of the stations used in this paper can be found in Table 1 and Figure 1a–c. The selected measurements were performed with different types of instruments that may differ substantially. When measurements are based on light absorption we refer to Equivalent BC (EBC), while measurements based on thermal-optical methods refer to elemental carbon (EC) (Petzold et al., 2013).

At Alert (ALT), Appalachian (APP), Asprveten (ASP), Birkenes (BIR), East Trout Lake (ETL), South Great Planes (SGP), Steamboat Springs (COL), Trinidad Head (TRI) and Whistler (WHI) measurements were performed with particle soot absorption photometers (PSAPs). At Annaberg-Buchholz (ANB), Bösel (BOS), Cabauw Zijdeweg (CAB), Hyytiälä (HYY), Leipzig (LEI), Melpitz (MEL), Nepal Climate Observatory (NEP), Pallas (PAL), Ústí n.L.-mesto (ULM) and Waldhof (WLD) the particle light absorption coefficient was measured by multi-angle absorption photometers (MAAP; Petzold and Schönlinner, 2004), which are in excellent agreement with other particle light absorption photometers such as a photoacoustic sensor (e.g., Muller et al., 2011). In the MAAP instrument, particles are continuously sampled on filter tape, with loaded spots subsequently analysed by Raman spectroscopy to derive the particle mass concentration of soot (Nordmann et al., 2013). The cut-off sizes of the different MAAP instruments varied between 1 and 10 µm. Continuous light absorption photometers (CLAP, Model PSAP; 565 nm) were used at Barrow (BAR), Bondville (BON), Gosan (GOS), K-puszta (KPU), BEO Moussala (MOU) and Summit (SUM). Although these instruments were calibrated to measure the aerosol absorption coefficient, a previous study at this site revealed that a value of 10 m^2 g^{-1} is a reasonable conversion factor to determine the BC concentration (Gelencsér et al., 2000). Aethalometers were used at Tiksi (TIK) and Zeppelin (ZEP).

All these stations measure the particle light absorption coefficients of different size fractions of the aerosol at wavelengths around 530–550 nm. Then the light absorption coefficients are converted to EBC mass concentrations under certain assumptions (Petzold et al., 2013). This is done externally for instruments such as MAAP, CLAP, PSAP etc. using a mass absorption efficiency of 10 m^2 g^{-1} (Bond and Bergstrom, 2006). For aethalometers, the conversion is done internally by the instrument. All station measurements are routinely filtered to remove influence from local sources.

2.2 Source – Receptor Relationships (SRRs)

We used the Lagrangian Particle Dispersion Model (LPDM), FLEXible PARTicle dispersion model (FLEXPART) (Stohl et al., 1998, 2005) to model atmospheric transport. Using LPDMs to model particle or trace gas concentrations has several advantages over Eulerian models, namely they can have quasi-infinite resolution and they are not subject to numerical diffusion. Thus they can provide better resolved source-receptor relationship (SRR) fields, which describe the relationship between the sensitivity of a "receptor" to a "source"

element, as described by Seibert and Frank (2004). SRRs for the lowest model level are often called footprint emission sensitivities or even just footprints.

SRRs were calculated using FLEXPART version 10 in a backwards mode (see Stohl et al., 2005) in which computational particles are released backward in time from the observation sites (receptors). When the number of observation sites is smaller than the number of unknown flux grid cells this mode is computationally more efficient than forward calculations. Furthermore, backward simulations can be initiated exactly at the measurement point without initial diffusion of information into a grid cell. This important advantage of LPDMs also facilitates high spatial resolution of the model output around the measurement sites. As meteorological input data, European Centre for Medium-Range Weather Forecasts operational meteorological analyses were used with 137 vertical levels and a horizontal resolution of 0.5°×0.5°. Retroplumes were calculated at hourly intervals at each of the receptors. 40,000 particles for each retroplume were released and followed 30 days backwards in time. This should be a sufficiently long time in order to include almost all contributions to BC concentration at the receptor given the atmospheric lifetime of BC (in the range of 2–10 days, Benkovitz et al., 2004; Koch and Hansen, 2005; Park et al., 2005; Textor et al., 2006).

The treatment of scavenging is a major uncertainty for modelling BC (Browse et al., 2012). Therefore, an ensemble of 12 model simulations was performed each with different BC tracers having different in–cloud and below–cloud scavenging properties (Table 2). This method allows the sensitivity of the SRRs (produced by FLEXPART) to scavenging to be quantified. Table 2 shows the different below–cloud and in–cloud scavenging parameters used within the model in the sensitivity runs. For all tracers, we assumed a logarithmic size distribution with an aerodynamic mean diameter of 0.25 μm, a logarithmic standard deviation of 0.3 and a particle density of 1500 kg m^{-3} (Long et al., 2013). The dry deposition scheme in FLEXPART is based on the resistance analogy (Slinn 1982). The present version of the model uses the precipitation rate from ECMWF to determine below-cloud scavenging and the cloud liquid water and ice content, precipitation rate and cloud depth from ECMWF to calculate in-cloud scavenging (see Grythe et al., 2017).

The SRR at the lowest model layer (in seconds) (Figure 1g–i) can be multiplied with gridded emission fluxes from a BC emission inventory (in kg m^{-2} s^{-1}) distributed over the layer depth (100 m). This gives the prior concentration of BC at the receptor point (in ng m^{-3}).

Atmos. Chem. Phys. Discuss., https://doi.org/10.5194/acp-2018-643
Manuscript under review for journal Atmos. Chem. Phys.
Discussion started: 23 July 2018

2.3 Bayesian inversion

The inversion methodology used in the present study, FLEXINVERT, is described fully in Thompson and Stohl (2014) and has been already used in studies of CH_4, HFC-125, HFC-134a and SF_6 (Brunner et al., 2017; Thompson et al., 2015, 2017). Since atmospheric transport and deposition are linear operations, they can be described as a Jacobian matrix of SRRs (**H**). The BC concentrations ($\boldsymbol{y}$) can then be modelled given an estimate of the emissions ($\boldsymbol{x}$) as follows:

$$\boldsymbol{y} = \mathbf{H}(\boldsymbol{x}) + \boldsymbol{\varepsilon} \qquad (1)$$

where $\boldsymbol{\varepsilon}$ is an error associated with model representation, such as the modelled transport and deposition as well as the measurements. Since **H** is generally not invertible (or may have no unique inverse), statistical optimization methods are used, which require prior information for regularization. According to Bayesian statistics, the problem can be expressed as the maximization of the probability density function of the emissions given the prior information and observations and is equivalent to finding the minimum of the cost function:

$$\mathbf{J}(\boldsymbol{x}) = \frac{1}{2}(\boldsymbol{x} - \boldsymbol{x_b})^{\boldsymbol{T}}\mathbf{B}^{-1}(\boldsymbol{x} - \boldsymbol{x_b}) + \frac{1}{2}(\boldsymbol{y} - \mathbf{H}\boldsymbol{x})^{\boldsymbol{T}}\mathbf{R}^{-1}(\boldsymbol{y} - \mathbf{H}\boldsymbol{x}) \qquad (2)$$

where **B** and **R** are the error covariance matrices for the prior emissions and the observations, respectively. The error in the observation space also accounts for model representation errors that are not related to the BC emissions. The emissions that minimize the cost function can be found by solving the first order derivative of equation (2). Hence, the following equation can be derived for the most probable emissions, $\boldsymbol{x}$ (for details see e.g. Tarantola, 2005):

$$\boldsymbol{x} = \boldsymbol{x_b} + \mathbf{B}\mathbf{H}^{\mathbf{T}}(\mathbf{H}\mathbf{B}\mathbf{H}^{\mathbf{T}} + \mathbf{R})^{-1}(\boldsymbol{y} - \mathbf{H}\boldsymbol{x_b}) \qquad (3)$$

In this study, the state vector contains the monthly unknown surface emissions on the grid of variable resolution (Figure 1d–f) and has a resolution of between 1.0°×1.0° and 8.0°×8.0°. The total number of emission variables to be determined was 1422 for 2013, 1404 for 2014 and 1436 for 2015. The posterior error covariance matrix, **A**, is equivalent to the inverse of the second derivative of the cost function. However, to account for the uncertainty in the scavenging parameters and different prior information, we instead conduct ensemble of inversions to estimate the posterior uncertainty in order to account for the systematic errors. To do this, we conduct the inversion for BC represented by 12 different scavenging coefficients (see Table 2) and for four different prior emission datasets, and do this for each of the three years of our study (2013–2015). The resulting model ensemble (12×4=48) for each year defines the posterior uncertainty due to scavenging and use of different a priori information (section 3.3).

Since negative values for the posterior emissions are mathematically possible but physically unlikely, we applied a subsequent inequality constraint on the emissions following the method of Thacker (2007). This is a truncated Gaussian approach in which inequality constraints are applied as error-free "observations":

$$\hat{\boldsymbol{x}} = \boldsymbol{x} + \mathbf{A}\mathbf{P}^{\mathbf{T}}(\mathbf{P}\mathbf{A}\mathbf{P}^{\mathbf{T}})^{-\mathbf{1}}(\boldsymbol{c} - \mathbf{P}\boldsymbol{x}) \quad (4)$$

where **A** is the posterior error covariance matrix, **P** is a matrix operator to select the variables that violate the inequality constraint, and $\boldsymbol{c}$ is a vector of the inequality constraint, which in this case is zero.

The emissions were solved on an irregular grid, which has been optimized based on the SRRs to give higher resolution (1.0° × 1.0°) in regions where there is strong contribution from emission sources to BC concentrations and lower (8.0° × 8.0°) where there is a weak contribution (Stohl et al., 2009). Then, the results are interpolated onto a uniform grid of 1.0°×1.0° resolution from 180°W to 180°E and 50°N to 90°N and are given at monthly time resolution for 2013, 2014 and 2015. To constrain emissions of BC monthly, a temporal correlation scale length between flux time-steps equal to 90 days was set.

2.4 A priori emission information

In the present study, the emission inventories ECLIPSE (Evaluating the CLimate and Air Quality ImPacts of ShortlivEd Pollutants) version 5 (Klimont et al., 2017) (available here: http://www.iiasa.ac.at/web/home/research/researchPrograms/air/Global_emissions.html), EDGAR (Emissions Database for Global Atmospheric Research) version HTAP_V2.2 (Janssens-Maenhout et al., 2015) (available here: http://edgar.jrc.ec.europa.eu/methodology.php#), ACCMIP (Emissions for Atmospheric Chemistry and Climate Model Intercomparison Project) version 5 (Lamarque et al., 2013) (available here: http://accent.aero.jussieu.fr/ACCMIP_metadata.php) and MACCity (Monitoring Atmospheric Composition & Climate / megaCITY - Zoom for the ENvironment) (Wang et al., 2014) (available here: http://accent.aero.jussieu.fr/MACC_metadata.php) were used as the prior emission estimates of BC (see Figure 2).

The ECLIPSE emission inventory (Figure 2a) accounts for waste burning, industrial combustion and processing, surface transportation that also includes power plants, energy conversion and extraction that also includes gas flaring, residential and commercial combustion.

The HTAP_V2 dataset (Figure 2b) consists of high-resolution gridded emissions of BC based on nationally reported emissions combined with regional scientific inventories. It

includes the sources of aviation, inland waterways and marine shipping, energy production other than electricity generation, industrial processes, solvent production and application, electricity generation, ground transport, buildings heating, cooling, equipment, and waste disposal or incineration.

The ACCMIP simulations use the BC emission inventory covering the historical period (1850–2000) provided by (Lamarque et al., 2010), which is built for the climate model simulations in CMIP5 (Figure 2c). Anthropogenic emissions are mainly based on Bond et al. (2004) but apply new emission factors. The year 2000 dataset was used for harmonization with the future emissions determined by Integrated Assessment Models (IAMs) for the four Representative Concentration Pathways (RCP4.5, RCP6, and RCP8.5). They include emissions from energy production and distribution, industry (combustion and non-combustion), transportation, maritime transport and aviation, residential and commercial combustion and solvent extraction, agricultural production and waste treatment.

MACCity (Figure 2d) was built as an extension of the historical emissions dataset of ACCMIP. It provides monthly averaged sectorial emissions for each year during the 1960-2010 period. This dataset was based on the decadal ACCMIP emissions for 1960-2000 and the 2005 and 2010 emissions provided by RCP 8.5. This scenario was chosen since it included some information on recent emissions at the regional scale in Europe and North America. The emission sectors are consistent with Lamarque et al. (2010).

Emissions from biomass burning were adopted from the Global Fire Emissions Database, Version 4 (GFEDv4) (Giglio et al., 2013) and implemented to each of the four emission inventories for 2013, 2014 and 2015. Emissions from gas flaring are only included in ECLIPSEv5 inventory.

3 Results

3.1 Sensitivity to scavenging and selection of the best representative species for BC

The comparison of the simulated and observed concentrations for the 12 different BC tracers (see Table 2) is shown in Taylor diagrams in Figure 3 for ECLIPSEv5 and in Figure S 1 for ACCMIPv5, EDGAR_HTAPv2.2 and MACCity, only for those stations that had continuous measurements for all the years of our study (2013–2015) namely ZEP, SUM, TIK, BAR, PAL, CAB, MEL and LEI (see Table 1). For all the different BC species,

concentrations of BC were calculated using the FLEXPART SRR and the four different emission datasets for 2013, 2014 and 2015.

Correlations of modelled and observed surface concentrations of BC were high (>0.5) only at stations ALT, MEL and LEI that present low NSD values (<1) and low nRMSE values. All NSD values were below 1.5 except at TIK and ULM stations (see Figure 3 and Figure S 1). In general, dispersion models fail to reproduce BC concentrations close to TIK station (Eckhardt et al., 2015; Evangeliou et al., 2016), as the station has been reported to receive pollution from local anthropogenic sources (Asmi et al., 2016). ULM station is located on the border between Germany and the Czech Republic and was shown previously to be strongly affected by BC emissions from residential combustion sources (Schladitz et al., 2015). The model-observation mismatches ($[model - observations]/observations$) due to the use of 12 different species for BC can be seen in Figure S 2 for the years 2013, 2014 and 2015. These values are average concentrations from the use of the four different emissions inventories (ECLIPSEv5, ACCMIPv5, EDGAR_HTAPv2.2 and MACCity). The extreme perturbation of the scavenging coefficients of BC caused an average relative model-observation mismatch (normalised against observations) of about 39% in 2013 (Figure S 2) at all stations.

Similar to 2013, 12 species with different scavenging parameters were used for BC following Table 2 in 2014 and the comparison with observations is shown in Taylor diagrams in Figure 3 using ECLIPSEv5 emissions and in Figure S 1 using ACCMIPv5, EDGAR_HTAPv2.2 and MACCity for the common stations. The comparison of surface simulated concentrations with observations showed NSD values above one, high nRMSE values and correlation coefficients below 0.5 in at most of the stations. The main difference from year 2013 is that the model-observation mismatches for the surface concentrations of the 12 BC species was estimated to be 32% in 2014 (Figure S 2), in contrast to 39% in 2013. The same deficiency of the model to capture the spring and summer concentrations of BC was observed. The calculated mismatches were very low in at most of the lower latitude stations and increased towards the remote Arctic ones (Figure S 2).

Finally, in 2015 the comparison of surface concentrations for each of the 12 different BC species using the four different datasets (ECLIPSEv5, ACCMIPv5, EDGAR_HTAPv2.2 and MACCity) with observations showed again the same pattern as in the previous years with most of the NSD values to be above unity, high nRMSE values and low Pearson coefficients (Figure 3 and Figure S 1). The model-observation mismatches of BC concentrations (Figure S 2) were estimated as high as 43% for the stations where full measurements existed for the

three years of the study (2013–2015). Like in the previous years, the model failed to reproduce surface concentrations of BC at some of the remote stations of the Arctic.

We used the NMSE (Normalised Mean Square Error) to select the most representative BC tracer species. The NMSE is an estimator of the overall deviations between predicted and measured values. It is defined as:

$$NMSE = \frac{1}{N}\sum_i \frac{(O_i - P_i)^2}{\bar{P}_i \bar{O}_i} \qquad (5)$$

where O_i and P_i are observed and predicted concentrations, N the number of observations for which we assess the predicted values, while the overbar indicates the mean over the number of observations for O_i and P_i. Contrary to the relative mismatches, in the NMSE the squared deviations (absolute values) are summed instead of the differences. For this reason, the NMSE generally shows the most striking differences among models. NMSE is a highly selective statistical quantity that can give large differences between models that perform similarly for other statistical measures. The lower the NMSE value, the better the performance of the model. On the other hand, high NMSE values do not necessarily mean that a model is completely wrong as the errors could be due to shifts in time and/or space. Moreover, it must be pointed out that NMSE is sensitive to outliers (Poli and Cirillo, 1993).

The calculated monthly average NMSE values for the 12 species using ECLIPSEv5 as the emission input can be seen in Figure 4 for year 2013–2015. The different scavenging coefficients used did not create a large variation in the monthly concentrations of BC. The best performance for the majority of the stations examined and most months was obtained for species 1, 2 and 10 (see Table 2). In terms of model response over the Arctic stations, a better performance was achieved for species 1 than for the other two. Therefore, we have chosen species 1 as our reference species for all subsequent analyses and the inversions. It should be noted here that the same test was performed using ACCMIPv5, EDGAR_HTAPv2.2 and MACCity emissions. Although the results were worse, the best-performed species for BC were again 1, 2 and 10.

3.2 Sensitivity to different prior information and selection of the best prior emission inventory

In this section we assess the impact of using the different prior emission inventories for BC and select the most appropriate one for our BC inversions. For this analysis, the best performing species 1 for BC (see Table 2) was chosen and the monthly relative model – observation mismatches ($([model - observations]/observations$) for all stations and years separated were calculated using all four inventories and are depicted in Figure S 3.

329 The largest monthly relative model-observation mismatches for the a priori simulated
330 concentrations of BC in 2013 were calculated for stations located close to 50°N (BOS, CAB
331 MEL, LEI, ULM, ANB). The average model-observation mismatch for all stations was 15%
332 for 2013. Similar results were found for 2014 for the prior simulated BC concentrations with
333 the largest relative mismatches recorded at mid-latitude stations where the BC concentrations
334 were very high due to large anthropogenic emissions (BOS, CAB, MEL, LEI). On average,
335 the relative model-observation mismatch was as high as 23% for the year 2014. Finally, in
336 2015, again the highest monthly relative mismatches of the a priori BC concentrations were
337 estimated for the stations of high anthropogenic influence (CAB, MEL, LEI, WLD). The
338 average relative model-observation mismatch in 2015 was only 19%, much lower than all
339 previous years. The fact that all prior emission datasets used failed to reproduce the
340 observations in central Europe during all years studied (2013, 2014 and 2015), whereas other
341 stations at mid-latitudes were reproduced well, might imply either missing sources or highly
342 uncertain measurements (Figure S 3). The use of different emission dataset changes simulated
343 concentrations by 23% at maximum.
344 NMSE values calculated for each of the four emission inventories were very low at the
345 majority of the stations for which data existed in all the years of study (ZEP, SUM, TIK,
346 BAR, MEL and LEI), when ECLIPSEv5 emissions were used, while at PAL all emission
347 datasets performed well (Figure 5). At most of the Arctic stations, the simulations using
348 ECLIPSEv5 reproduced the observations better compared to the other inventories examined.
349 This shows that the most appropriate emission dataset for our purpose is the ECLIPSEv5
350 inventory, as it is the only one that can capture the characteristically elevated concentrations
351 of BC in the Arctic, which persist until spring, and are caused by anthropogenic emissions
352 (Law and Stohl, 2007). A significant deficiency is found for TIK for reasons that were
353 explained earlier (see section 3.1).

354 **3.3 Optimised (a posteriori) emissions of BC and associated uncertainty**

355 The optimised annual emissions of BC together with the associated posterior gridded
356 uncertainty and the difference between posterior and prior emissions averaged for the 2013–
357 2015 period can be seen in Figure 6. The posterior emissions were calculated for the best
358 performing species (species 1) of BC and the best prior emissions inventory (ECLIPSEv5).
359 The total posterior uncertainty was calculated as the standard deviation of the posterior
360 emissions calculated for the 12 BC species with different scavenging coefficients for four
361 different emission datasets as prior information for each of the three years (12×4=48

inversions, see section 2.2). The total uncertainty is a combination of the deposition uncertainty (represented by the posterior emissions using 12 perturbed BC species with different scavenging coefficients) and the uncertainty due to the use of different prior information (represented by the posterior emissions using the four different emission datasets). Table 3 reports annual prior and posterior emissions of BC for different regions and average emissions for the period 2013–2015. Five different regions are accounted for, namely North America, North Europe (including European Russia), North Siberia, Nenets-Komi (Russia) and Khanty-Mansiysk district (Russia).

The optimised emissions show some constant hot-spot areas that persist throughout all three years and which are attributed to anthropogenic emissions of BC. For instance, emissions in the Nenets – Komi region close to the Yamal peninsula in Russia or in Khanty Mansiysk region of Northwestern Siberia have been reported to originate to a large extent from gas flaring (Popovicheva et al., 2017; Stohl et al., 2013; Winiger et al., 2017). Other areas that are characterised by large anthropogenic emissions are in Western Canada (Alberta), where more than 100 power industries burn fossil fuels and more than 50 oil and gas production and oil refining industries operate. In addition, one of the largest oil sands deposits are found in Northern Alberta and in the McMurray area, which contains about 168 billion barrels of oil (Heins, 2000). Cheng et al. (2018) found high concentrations of BC (more than 1000 ng m^{-3}) in the Canadian oil sands region at altitudes of up to 2 km during a flight campaign.

The optimised emissions of BC in North America for the 2013–2015 period were between 149 and 193 kt y^{-1} (average ± 1-sigma error: 174±58 kt y^{-1}), in the same order with the prior emissions in ECLIPSEv5 (148–182 kt y^{-1}) and slightly higher than ACCMIPv5, EDGAR_HTAPv2.2 and MACCity (116–150 kt y^{-1}). In Northern Europe we estimated that 124–238 kt y^{-1} of BC were released (average ± 1-sigma error: 170±59 kt y^{-1}), which is less than half the ECLIPSEv5 emissions (352–381 kt y^{-1}), about 35% lower than the ACCMIPv5 and MACCity emissions (241 – 256 kt y^{-1}) and in the same order as the EDGAR_HTAPv2.2 emissions (163–175 kt y^{-1}). Posterior emissions of BC were higher in North Siberia for the 3-year period (130–291 kt y^{-1}, average ± 1-sigma error: 217±69 kt y^{-1}) compared with ECLIPSEv5 (187–238 kt y^{-1}), ACCMIPv5 (127–178 kt y^{-1}), EDGAR_HTAPv2.2 (108–159 kt y^{-1}) or MACCity (129–179 kt y^{-1}). Larger changes in the emissions of BC were calculated in Russian territories that are known to be important gas flaring sources (Stohl et al., 2013). Emissions of BC in the Nenets-Komi oblast were between 14 and 17 kt y^{-1} (average ± 1-sigma error: 15±5 kt y^{-1}), about 40% lower than the respective emissions in ECLIPSEv5 (≈25

kt y^{-1}), the only prior dataset that took gas flaring into account there. This could be due to the decreasing magnitude of the flaring emissions in the last few years (see Huang and Fu, 2016). Finally, in Khanty-Mansiysk emissions of BC were 28–37 kt y^{-1} (average ± 1-sigma error: 32±8 kt y^{-1}) compared to 25 kt yr^{-1} in ECLIPSEv5, whereas in the other datasets that do not include emissions of BC due to flaring, BC emissions were negligible. However, the posterior Khanty-Mansiysk emissions are shifted further east compared to the prior.

The annual posterior emissions of BC at latitudes above 50°N were estimated as 560±171 kt yr^{-1} averaged for the 2013–2015 time period (523±92 kt yr^{-1} in 2013, 608±104 kt yr^{-1} in 2014 and 549±100 kt yr^{-1} in 2015, respectively). For the same area and period, BC emissions in ECLIPSEv5 were 745 kt yr^{-1}, in ACCMIPv5 533 kt yr^{-1}, in EDGAR_HTAPv2.2 437 kt yr^{-1}, while in MACCity they were 538 kt yr^{-1}. The annual posterior absolute uncertainty can be seen in Figure 6b. As it was explained before, this uncertainty is a combination of the uncertainty due to scavenging and due to the use of different prior information in the inversions of BC. The relative uncertainty of the inversion averaged over the period 2013 to 2015 was estimated to be 30%. The uncertainty due to different scavenging coefficients in the BC species used was 25%, while the uncertainty due to the use of different prior emissions was only 5%.

3.4 Validation of the posterior emissions of BC

The concentrations of BC at eight measurement stations simulated with the posterior (optimised) emissions of BC can be seen in Figure S 4. As expected, BC concentrations match the observations significantly better than using any of the a priori datasets with correlation coefficients above 0.6 for most of the stations. At the same time, NSD values were close to unity or lower and the nRMSE values below 1.5 at most of the stations shown in Figure S 4. However, the comparison to observations included in the inversion is not a sufficient indicator of the inversion's performance, as the inversion is designed to reduce the model-observation mismatches. The magnitude of the posterior reduction of the model mismatch to the observations is partly determined by the weighting given to the observations relative to the prior emissions. A much better performance indicator is the comparison of the posterior concentrations with observations that were not included in the inversion (independent observations).

For this reason, we compared posterior BC concentrations with observations from the ACCACIA (Aerosol-Cloud Coupling and Climate Interactions in the Arctic) flight campaign, which was conducted near Zeppelin station, Ny-Ålesund, for 3 days in March 2013 (Sinha et

al., 2017). This campaign was chosen because it was conducted during one year for which inversion results are available (2013). The results are shown in Figure 7 for the prior simulated concentrations of BC using four different emission datasets (ACCMIPv5, ECLIPSEv5, EDGAR_HTAPv2.2 and MACCity) and the posterior simulated BC concentrations. In all profiles, use of the optimised emissions of BC results in a better agreement between modeled concentrations and observations compared to the prior simulated BC concentrations, while the RMSE (not normalised) values decrease substantially. However, the Pearson's correlation coefficients were below 0.5.

To assess the performance of the inversions of BC in 2014, we used an independent dataset from a ship campaign that took place in the North Atlantic and Baltic Seas in June and August 2014 (Figure 8) provided by Shevchenko et al. (2016). Although the measurements may sometimes be affected by the ship's exhaust, the posterior RMSE was 34% lower than the average RMSE using four different a priori emission datasets (ACCMIPv5, ECLIPSEv5, EDGAR_HTAPv2.2 and MACCity), supporting the view that the inversion improved the emissions for 2014.

To validate the 2015 inversions of BC, measurements from a ship campaign over the Russian Arctic were used (Popovicheva et al., 2017) and the results are shown in Figure 9. The cruise started from the port of Arkhangelsk in the Northwestern European Russia, reached the Bolshevik Island in the higher Russian Arctic and returned following more or less the same pathway. The calculated RMSE of the posterior BC concentrations with the measurements taken during the cruise was about 10% lower that the respective RMSE from the prior simulated concentrations of BC (average for all prior simulated emissions). This shows that the optimised emissions improved BC concentrations over the Russian Arctic. Some episodic peaks of BC throughout the ship cruise, however, were poorly captured.

4 Discussion

4.1 BC emissions in North America

The spatial distribution of the optimised emissions of BC in North America averaged for the 3-year period is depicted in Figure 10 and the annual posterior emissions for 2013, 2014 and 2015 are shown in Figure S 5. In the same figures the differences between posterior and prior emissions (ECLIPSEv5) are shown (right panels) to indicate the biggest emission changes compared to the a priori dataset.

The most characteristic locations of sources between 2013 and 2015 lie in Alberta, where most of the large oil-producing industries operate (Figure 10 and Figure S 5). The highest emission source was seen in 60°N–135°W in 2013 and 2015, but not in 2014. This spot corresponds to the location of Whitehorse, which is the capital and only city of Yukon, and the largest city in Northern Canada. The area involves mining activities (mainly for gold) and three natural gas wells, while biomass in the form of cordwood and pellets is used for space heating (Yukon Government, 2018). The fact that near-zero emissions of BC were calculated in Whitehorse in 2014 might be due to the lack of available measurements in North America, which in turn results in poorly constrained posterior emissions of BC. Another similar hotspot area that is more intense in 2013 and 2015, but not in 2014 is located in Yellowknife north of Great Slave Lake (62.5°N–115°W, Figure S 5). The city is known for gold and diamond mining and an oil-driven power plant (Northwest Territories Power Corporation, https://www.ntpc.com). Finally, another characteristic hotspot emission region of BC is seen southeast of Lake Athabasca (57°N–108°W, Figure 10). In this region four uranium mines are located that use diesel generators, diesel trucks, and likely also other diesel-powered machinery. Exactly in this location, the Visible Infrared Imaging Radiometer Suite (VIIRS) showed relatively strong night-time light sources (https://www.lightpollutionmap.info/#zoom=5&lat=8255540&lon=-11864816&layers=B0FFFTFFFT).

4.2 BC emissions in Northern Europe

The posterior emissions of BC in Northern Europe averaged for the period 2013–2015 can be seen in Figure 11 together with the difference between prior (ECLIPSEv5) and posterior BC emissions, while the posterior emissions for each individual year are shown in Figure S 6. The location of the gas flaring facilities are also presented in the same figures together with vegetation fires from the FEINE (Fire Emission Inventory– northern Eurasia) inventory (Hao et al., 2016). The latter combines the MODIS thermal anomalies products (MOD14 and MYD14) and the MODIS top-of-the-atmosphere-calibrated reflectance product (MOD02) to map and date burn scars that are screened for false detections. Land cover classification of burned areas are taken from the MODIS land cover change product (MOD12) (Friedl et al., 2010). This dataset is considered more realistic than GFED4 due to the emission factors used for BC (May et al., 2014) and the different approach of burned area calculation (see Hao et al., 2016).

493 The highest posterior emissions of BC are calculated for the Moscow megacity at
494 55°N–37.5°E, Berlin 52°N–14°E, Warsaw 52°N–21°E, Kyiv 50°N–30°E, Saint Petersburg
495 60°N–30°E, while London is slightly misplaced to the west (Figure 11). The Scandinavian
496 countries have the lowest emissions, although domestic heating there can also be important
497 (Andersen and Jespersen, 2016). The difference between prior and posterior emissions show
498 that vegetation fires have a large impact on the BC emissions especially in Eastern Europe. In
499 particular in 2015, the inversion produces large emission increases exactly where a large
500 number of fire hot spots were found (see Figure S 6).

501 **4.3 BC emissions in North Siberia**

502 Figure 12 illustrates the average posterior emissions of BC in Western Siberia for the
503 2013–2015 period together with the difference between the prior (ECLIPSEv5) and the
504 posterior emissions of BC, while Figure S 7 shows the respective emissions of BC for each
505 year individually, together with the flaring facilities and the vegetation fires similarly to the
506 previous section.

507 The prior emissions of BC from flaring in Nenets-Komi oblast are confirmed by the
508 inversion, although the emissions are shifted further east, while the flaring emissions in
509 Khanty-Mansiysk are probably underestimated in ECLIPSEv5 (see also Table 3). Vegetation
510 fires are shown to correlate well with BC emissions for 2013 (60°N –70°N) and 2014 (50°N–
511 60°N) (Figure S 7), but not in 2015. Hotspots of high emissions were found in Dudinka
512 (88°E–70°N), a town on the Yenisei River and the administrative center of Taymyrsky
513 Dolgano-Nenetsky District of Krasnoyarsk Krai, Russia, due to the Norilsk Mining and
514 Smelting Factory extracting coal and ores. Furthermore, increase posterior emissions of BC
515 were estimated across the line that connects some important Russian cities (Yekaterinsburg to
516 Chelyabinsk, 60°E–55°N). These cities have been reported to contribute large amounts of BC
517 mainly from transportation (see Evangeliou et al., 2018). Another hotspot exists at 108°E–
518 58°N that corresponds to VIIRS night-time lights
519 (https://www.lightpollutionmap.info/#zoom=5.696666666666656&lat=8239438&lon=12096
520 227&layers=B0FFFTFFFT). These emissions are attributed to flaring as four facilities are
521 collocated there (see Figure 12). Finally, high emissions of BC originate from the Nizhny
522 Novgorod oblast (44°E–55°N). The oblast ranks seventh in Russia in industrial output.
523 Processing industries predominate in the local economy. The leading sectors of more than 650
524 industries are engineering and metalworking, followed by chemical and petrochemical

industries and forestry, woodworking, and paper industries and one facility that flare gas (GGFR, Figure 12).

In the western part of Siberia, there are numerous sources of average or low intensity. However, there no known anthropogenic sources there. At the lowest part of the inversion domain, in the borders of Russia with Mongolia, the posterior emissions showed a large increase (Figure 6). These emissions are prevalent along the Trans-Siberian Railway. Human activities in the villages along the railway have been highlighted to be the major cause of the fires there.

4.4 Seasonal variability of BC emissions

The monthly optimised emissions of BC are shown in Figure 13 for the three years of study (2013–2015) for the entire area north of 50°N, and separately for areas north of 50°N in North America, North Europe, North Siberia, Nenets-Komi oblast (Russia) and Khanty-Mansiysk (Russia). The last two regions are known to have large emissions from gas flaring. In the same figure the prior emissions from ECLIPSEv5, EDGAR_HTAPv2.2, ACCMIPv5 and MACCity are plotted for comparison.

The total posterior emissions of BC (>50°N) show large seasonal variation (Figure 13a). The maximum emissions were calculated for summer months (July in 2013 and June in 2014 and 2015). In these months large emissions from biomass burning have been reported both in GFED4 (see burned area in Giglio et al., 2013), as well as in the FEINE inventory for Northern Eurasia (Hao et al., 2016). By separating the inversion domain into continental regions, it is easily seen where biomass burning is important. For instance, in North America (Figure 13b), although GFED4 that is included in all the prior emission datasets, shows a large emission peak for BC in summer implying that fires are important, our optimised emissions show a significantly smaller variability. This was not the case for North Europe (Figure 13c) where the largest seasonal emissions of BC were found in July for 2013 and in May for 2015, while in 2014 the largest peak was already in April. This is not seen in the prior emission datasets, which show weak monthly variation. The largest seasonal variations were calculated for Northern Siberia (Figure 13d) and emissions of BC there control the overall seasonal pattern for the total optimised emissions of BC (>50°N). A large month-to-month variability was estimated in the Nenets-Komi oblast (Figure 13e) likely as a consequence of errors in the inversion, but no clear seasonal pattern. Finally, the largest monthly emissions of BC in Khanty-Mansiysk oblast of Russia (Figure 13f) were calculated in April for 2013, July for 2014 and June for 2015 showing that a large share in the emissions

of BC in this region originate from biomass burning since the region is located at mid-latitudes (60°N–65°N) and is vulnerable to open fires.

5 Conclusions

We have optimised emissions of BC at high northern latitudes (>50°N) for the 2013–2015 period using a Bayesian inversion tool, an atmospheric transport model and network of continuous measurements of BC. We performed a sensitivity study to assess the best representative species for BC in terms of scavenging and removal and the best representative emission inventory to be used as the prior information for our inversion.

The perturbation of scavenging coefficients for BC in the simulated concentrations creates a relative model–observation mismatch of 32%–43% for the three years of study, whereas the use of different emission inventories has a less significant effect in the simulated concentrations showing a relative model–observation mismatch of 15%–23%.

The posterior emissions of BC show characteristic hot-spots throughout all three years in the Nenets – Komi region close to the Yamal peninsula in Russia or in Khanty Mansiysk region of Northwestern Siberia, where gas flaring facilities are located and in Western Canada (Alberta), where more than 150 power and oil/gas production industries operate. The annual posterior emissions of BC at latitudes above 50°N were estimated as 560±171 kt yr^{-1}, significantly smaller than in ECLIPSEv5 (745 kt yr^{-1}), which was used and the prior information in the inversions of BC (best representative emission dataset).

The uncertainty of the inversions was assessed using a model ensemble represented by 12 different scavenging coefficients for BC and four different prior emission datasets (12×4=48) for each of the three years of our study. We calculate a relative uncertainty of the inversion of 30% for the three years of our study.

The posterior simulated concentrations of BC showed a better agreement with independent observations adopted from flight and ship campaigns over the Arctic presenting, in all cases, up to three times lower RMSE values.

In North America, the posterior emissions were found similar to the a priori ones driven by anthropogenic sources, while biomass burning appeared to be insignificant. This was confirmed by satellite products that showed weak existence of active fire hot-spots.

In North Europe, posterior emissions were estimated to be half compared to the prior ones, with the highest releases to be in megacities and due to biomass burning in Eastern Europe.

590 Finally, in North Siberia the larger emissions were calculated along the transect
591 between Yekaterinsburg and Chelyabinsk, while flaring in Nenets-Komi oblast is probably
592 overestimated in the a priori emissions. Increased emissions in the borders between Russia
593 and Mongolia are probably due to biomass burning in villages along the Trans-Siberian
594 Railway.
595
596 *Data availability.* All data generated for the present publication are stored on NIRD
597 (https://www.uio.no/english/services/it/research/storage/nird-sigma.html) (project NS9419K)
598 and can be obtained from the corresponding author upon request.
599
600 *Competing financial interests.* The authors declare no competing financial interests.
601
602 *Acknowledgements.* We would like to acknowledge the project entitled "Emissions of
603 Short-Lived Climate Forcers near and in the Arctic (SLICFONIA)", which was funded by the
604 NORRUSS research program (Project ID: 233642) and the project entitled "The Role of
605 Short-Lived Climate Forcers in the Global Climate" funded by the KLIMAFORSK program
606 (Project ID: 235548) of the Research Council of Norway. Also the Research Council of
607 Norway strategic institute initiatives (SIS) project "SOCA-Signals from the Arctic OCean in
608 the Atmosphere" is acknowledged. We also acknowledge partial support by the AMAP
609 secretariat, as this work shall contribute to the next AMAP assessment on short-lived climate
610 forcers. Work was performed at the Nordic Centre of Excellence eSTICC (eScience Tools for
611 Investigating Climate Change in northern high latitudes), supported by NordForsk grant
612 57001. We thank IIASA (especially Chris Heyes and Zig Klimont) for providing the
613 ECLIPSEv5 emission dataset for BC. Computational and storage resources for the
614 FLEXPART simulations were provided by NOTUR (NN9419K) and NIRD (NS9419K). All
615 results can be accessed upon request to the corresponding author of this manuscript.
616
617 *Author contributions.* NE performed the simulations, analyses and wrote the paper, RLT
618 helped in the adaptation of FLEXINVERT for BC and commented on the paper, SE helped in
619 the implementation of the experiments and AS coordinated, commented and wrote parts of
620 the paper.
621
622 **References**
623 Ackerman, a. S.: Reduction of Tropical Cloudiness by Soot, Science (80-.)., 288(5468),

624 1042–1047, doi:10.1126/science.288.5468.1042, 2000.
625 AMAP: AMAP assessment 2015: Black carbon and ozone as Arctic climate forcers, Arctic
626 Monitoring and Assessment Programme (AMAP), Oslo, Norway., 2015.
627 Andersen, S. and Jespersen, M. G.: A Protocol for Measuring Emissions of Black Carbon and
628 Organic Carbon from Residential Wood Burning. [online] Available from:
629 http://webcache.googleusercontent.com/search?q=cache:T48eUfM_V6YJ:www.ccacoalition.
630 org/en/file/2570/download%3Ftoken%3DNkBK2GWw+&cd=3&hl=no&ct=clnk&gl=no&cli
631 ent=safari, 2016.
632 Asmi, E., Kondratyev, V., Brus, D., Laurila, T., Lihavainen, H., Backman, J., Vakkari, V.,
633 Aurela, M., Hatakka, J., Viisanen, Y., Uttal, T., Ivakhov, V. and Makshtas, A.: Aerosol size
634 distribution seasonal characteristics measured in Tiksi, Russian Arctic, Atmos. Chem. Phys.,
635 16(3), 1271–1287, doi:10.5194/acp-16-1271-2016, 2016.
636 Benkovitz, C. M., Schwartz, S. E., Jensen, M. P., Miller, M. A., Easter, R. C. and Bates, T. S.:
637 Modeling atmospheric sulfur over the Northern Hemisphere during the Aerosol
638 Characterization Experiment 2 experimental period, J. Geophys. Res. D Atmos., 109(22), 1–
639 28, doi:10.1029/2004JD004939, 2004.
640 Bond, T. C. and Bergstrom, R. W.: Light Absorption by Carbonaceous Particles: An
641 Investigative Review, Aerosol Sci. Technol., 40(1), 27–67, doi:10.1080/02786820500421521,
642 2006.
643 Bond, T. C., Streets, D. G., Yarber, K. F., Nelson, S. M., Woo, J. H. and Klimont, Z.: A
644 technology-based global inventory of black and organic carbon emissions from combustion, J.
645 Geophys. Res. D Atmos., 109(14), 1–43, doi:10.1029/2003JD003697, 2004.
646 Bond, T. C., Doherty, S. J., Fahey, D. W., Forster, P. M., Berntsen, T., Deangelo, B. J.,
647 Flanner, M. G., Ghan, S., Kärcher, B., Koch, D., Kinne, S., Kondo, Y., Quinn, P. K., Sarofim,
648 M. C., Schultz, M. G., Schulz, M., Venkataraman, C., Zhang, H., Zhang, S., Bellouin, N.,
649 Guttikunda, S. K., Hopke, P. K., Jacobson, M. Z., Kaiser, J. W., Klimont, Z., Lohmann, U.,
650 Schwarz, J. P., Shindell, D., Storelvmo, T., Warren, S. G. and Zender, C. S.: Bounding the
651 role of black carbon in the climate system: A scientific assessment, J. Geophys. Res. Atmos.,
652 118(11), 5380–5552, doi:10.1002/jgrd.50171, 2013.
653 Browse, J., Carslaw, K. S., Arnold, S. R., Pringle, K. and Boucher, O.: The scavenging
654 processes controlling the seasonal cycle in Arctic sulphate and black carbon aerosol, Atmos.
655 Chem. Phys., 12(15), 6775–6798, doi:10.5194/acp-12-6775-2012, 2012.
656 Brunner, D., Arnold, T., Henne, S., Manning, A., Thompson, R. L., Maione, M., Doherty, S.
657 O. and Reimann, S.: Comparison of four inverse modelling systems applied to the estimation

658 of HFC-125 , HFC-134a , and SF 6 emissions over Europe, , 10651–10674, 2017.
659 Cao, G., Zhang, X. and Zheng, F.: Inventory of black carbon and organic carbon emissions
660 from China, Atmos. Environ., 40(34), 6516–6527, doi:10.1016/j.atmosenv.2006.05.070,
661 2006.
662 Cheng, Y., Li, S., Gordon, M. and Liu, P.: Size distribution and coating thickness of black
663 carbon from the Canadian oil sands operations, , 2004, 2653–2667, 2018.
664 Clarke, A. D. and Noone, K. J.: Soot in the arctic snowpack: a cause for perturbations in
665 radiative transfer, Atmos. Environ., 41(SUPPL.), 64–72, doi:10.1016/0004-6981(85)90113-1,
666 1985.
667 Eckhardt, S., Quennehen, B., Olivié, D. J. L., Berntsen, T. K., Cherian, R., Christensen, J. H.,
668 Collins, W., Crepinsek, S., Daskalakis, N., Flanner, M., Herber, A., Heyes, C., Hodnebrog,
669 Huang, L., Kanakidou, M., Klimont, Z., Langner, J., Law, K. S., Lund, M. T., Mahmood, R.,
670 Massling, A., Myriokefalitakis, S., Nielsen, I. E., Nøjgaard, J. K., Quaas, J., Quinn, P. K.,
671 Raut, J. C., Rumbold, S. T., Schulz, M., Sharma, S., Skeie, R. B., Skov, H., Uttal, T., Von
672 Salzen, K. and Stohl, A.: Current model capabilities for simulating black carbon and sulfate
673 concentrations in the Arctic atmosphere: A multi-model evaluation using a comprehensive
674 measurement data set, Atmos. Chem. Phys., 15(16), 9413–9433, doi:10.5194/acp-15-9413-
675 2015, 2015.
676 Elvidge, C. D., Ziskin, D., Baugh, K. E., Tuttle, B. T., Ghosh, T., Pack, D. W., Erwin, E. H.
677 and Zhizhin, M.: A fifteen year record of global natural gas flaring derived from satellite data,
678 Energies, 2(3), 595–622, doi:10.3390/en20300595, 2009.
679 Evangeliou, N., Balkanski, Y., Hao, W. M., Petkov, A., Silverstein, R. P., Corley, R.,
680 Nordgren, B. L., Urbanski, S. P., Eckhardt, S., Stohl, A., Tunved, P., Crepinsek, S., Jefferson,
681 A., Sharma, S., Nøjgaard, J. K. and Skov, H.: Wildfires in northern Eurasia affect the budget
682 of black carbon in the Arctic-a 12-year retrospective synopsis (2002-2013), Atmos. Chem.
683 Phys., 16(12), 7587–7604, doi:10.5194/acp-16-7587-2016, 2016.
684 Evangeliou, N., Shevchenko, V. P., Yttri, K. E., Sollum, E., Pokrovsky, O. S., Kobelev, V.
685 O., Vladimir, B., Lobanov, A. A., Starodymova, D. P., Vorobiev, S. N., Thompson, R. L.,
686 Stohl, A., Toulouse, G. E. and Belin, E.: Origin of elemental carbon in snow from Western
687 Siberia and northwestern European Russia during winter – spring, Atmos. Chem. Phys., 18,
688 963–977, doi:10.5194/acp-18-963-2018, 2018.
689 Friedl, M. A., Sulla-Menashe, D., Tan, B., Schneider, A., Ramankutty, N., Sibley, A. and
690 Huang, X.: MODIS Collection 5 global land cover: Algorithm refinements and
691 characterization of new datasets, Remote Sens. Environ., 114(1), 168–182,

692 doi:10.1016/j.rse.2009.08.016, 2010.
693 Gelencsér, A., Hoffer, A., Molnár, A., Krivácsy, Z., Kiss, G. and Mészáros, E.: Thermal
694 behaviour of carbonaceous aerosol from a continental background site, Atmos. Environ.,
695 34(5), 823–831, doi:10.1016/S1352-2310(99)00206-X, 2000.
696 Giglio, L., Randerson, J. T. and van der Werf, G. R.: Analysis of daily, monthly, and annual
697 burned area using the fourth-generation global fire emissions database (GFED4), J. Geophys.
698 Res. Biogeosciences, 118, 317–328, doi:10.1002/jgrg.20042, 2013, 2013.
699 Government, Y.: Economic sectors, 2018.
700 Grythe, H., Kristiansen, N. I., Groot Zwaaftink, C. D., Eckhardt, S., Ström, J., Tunved, P.,
701 Krejci, R. and Stohl, A.: A new aerosol wet removal scheme for the Lagrangian particle
702 model FLEXPARTv10, Geosci. Model Dev., 10, 1447–1466, doi:10.5194/gmd-10-1447-
703 2017, 2017.
704 Hao, W. M., Petkov, A., Nordgren, B. L., Silverstein, R. P., Corley, R. E., Urbanski, S. P.,
705 Evangeliou, N., Balkanski, Y. and Kinder, B.: Daily black carbon emissions from fires in
706 Northern Eurasia from 2002 to 2013, Geosci. Model Dev., 9, 4461–4474, doi:10.5194/gmd-9-
707 4461-2016, 2016.
708 Hegg, D. A., Warren, S. G., Grenfell, T. C., Doherty, S. J., Larson, T. V. and Clarke, A. D.:
709 Source attribution of black carbon in arctic snow, Environ. Sci. Technol., 43(11), 4016–4021,
710 doi:10.1021/es803623f, 2009.
711 Heins, F. J.: Historical overview of the Fort McMurray area and oil sands industry in
712 Northeast Alberta. [online] Available from:
713 https://web.archive.org/web/20080227201038/http://www.ags.gov.ab.ca/publications/ESR/P
714 DF/ESR_2000_05.pdf, 2000.
715 Hodnebrog, Ø., Myhre, G. and Samset, B. H.: How shorter black carbon lifetime alters its
716 climate effect., Nat. Commun., 5(May), 5065, doi:10.1038/ncomms6065, 2014.
717 Huang, K. and Fu, J. S.: A global gas flaring black carbon emission rate dataset from 1994 to
718 2012, Nature, 3, 160104, doi:10.1038/sdata.2016.104, 2016.
719 Huang, K., Fu, J. S., Prikhodko, V. Y., Storey, J. M., Romanov, A., Hodson, E. L., Cresko, J.,
720 Morozova, I., Ignatieva, Y. and Cabaniss, J.: Russian anthropogenic black carbon: Emission
721 reconstruction and Arctic black carbon simulation, J. Geophys. Res. Atmos., 120(21), 11306–
722 11333, doi:10.1002/2015JD023358, 2015.
723 Janssens-Maenhout, G., Crippa, M., Guizzardi, D., Dentener, F., Muntean, M., Pouliot, G.,
724 Keating, T., Zhang, Q., Kurokawa, J., Wankmüller, R., Denier Van Der Gon, H., Kuenen, J. J.
725 P., Klimont, Z., Frost, G., Darras, S., Koffi, B. and Li, M.: HTAP-v2.2: A mosaic of regional

and global emission grid maps for 2008 and 2010 to study hemispheric transport of air pollution, Atmos. Chem. Phys., 15(19), 11411–11432, doi:10.5194/acp-15-11411-2015, 2015.

Jinhuan, Q. and Liquan, Y.: Variation characteristics of atmospheric aerosol optical depths and visibility in North China during 1980 } 1994, Atmos. Environ., 34, 603–609, 2000.

Klimont, Z., Kupiainen, K., Heyes, C., Purohit, P., Cofala, J., Rafaj, P., Borken-Kleefeld, J. and Schöpp, W.: Global anthropogenic emissions of particulate matter including black carbon, Atmos. Chem. Phys., 17, 8681–8723, doi:10.5194/acp-17- 50 8681-2017, 2017.

Klonecki, A.: Seasonal changes in the transport of pollutants into the Arctic troposphere-model study, J. Geophys. Res., 108(D4), 8367, doi:10.1029/2002JD002199, 2003.

Koch, D. and Hansen, J.: Distant origins of Arctic black carbon: A Goddard Institute for Space Studies ModelE experiment, J. Geophys. Res. D Atmos., 110(4), 1–14, doi:10.1029/2004JD005296, 2005.

Lamarque, J. F., Bond, T. C., Eyring, V., Granier, C., Heil, A., Klimont, Z., Lee, D., Liousse, C., Mieville, A., Owen, B., Schultz, M. G., Shindell, D., Smith, S. J., Stehfest, E., Van Aardenne, J., Cooper, O. R., Kainuma, M., Mahowald, N., McConnell, J. R., Naik, V., Riahi, K. and Van Vuuren, D. P.: Historical (1850-2000) gridded anthropogenic and biomass burning emissions of reactive gases and aerosols: Methodology and application, Atmos. Chem. Phys., 10(15), 7017–7039, doi:10.5194/acp-10-7017-2010, 2010.

Lamarque, J. F., Shindell, D. T., Josse, B., Young, P. J., Cionni, I., Eyring, V., Bergmann, D., Cameron-Smith, P., Collins, W. J., Doherty, R., Dalsoren, S., Faluvegi, G., Folberth, G., Ghan, S. J., Horowitz, L. W., Lee, Y. H., MacKenzie, I. A., Nagashima, T., Naik, V., Plummer, D., Righi, M., Rumbold, S. T., Schulz, M., Skeie, R. B., Stevenson, D. S., Strode, S., Sudo, K., Szopa, S., Voulgarakis, A. and Zeng, G.: The atmospheric chemistry and climate model intercomparison Project (ACCMIP): Overview and description of models, simulations and climate diagnostics, Geosci. Model Dev., 6(1), 179–206, doi:10.5194/gmd-6-179-2013, 2013.

Law, K. S. and Stohl, A.: Arctic Air Pollution: Origins and Impacts, Science (80-.)., 315(5818), 1537–1540, doi:10.1126/science.1137695, 2007.

Long, C. M., Nascarella, M. A. and Valberg, P. A.: Carbon black vs. black carbon and other airborne materials containing elemental carbon: Physical and chemical distinctions, Environ. Pollut., 181, 271–286, doi:10.1016/j.envpol.2013.06.009, 2013.

May, A. A., McMeeking, G. R., Lee, T., Taylor, J. W., Craven, J. S., Burling, I., Sullivan1, A. P., Akagi, S., Jr., J. L. C., Flynn, M., Coe, H., Urbanski, S. P., Seinfeld6, J. H., Yokelson8, R. J. and Kreidenweis, S. M.: Aerosol emissions from prescribed fires in the United States: A

760 synthesis of laboratory and aircraft measurements, J. Geophys. Res. Atmos., 119, 11826–
761 11849, doi:10.1002/ 2014JD021848, 2014.
762 Muller, T., Henzing, J. S., De Leeuw, G., Wiedensohler, A., Alastuey, A., Angelov, H.,
763 Bizjak, M., Collaud Coen, M., Engstr??m, J. E., Gruening, C., Hillamo, R., Hoffer, A., Imre,
764 K., Ivanow, P., Jennings, G., Sun, J. Y., Kalivitis, N., Karlsson, H., Komppula, M., Laj, P., Li,
765 S. M., Lunder, C., Marinoni, A., Martins Dos Santos, S., Moerman, M., Nowak, A., Ogren, J.
766 A., Petzold, A., Pichon, J. M., Rodriquez, S., Sharma, S., Sheridan, P. J., Teinil??, K., Tuch,
767 T., Viana, M., Virkkula, A., Weingartner, E., Wilhelm, R. and Wang, Y. Q.: Characterization
768 and intercomparison of aerosol absorption photometers: Result of two intercomparison
769 workshops, Atmos. Meas. Tech., 4(2), 245–268, doi:10.5194/amt-4-245-2011, 2011.
770 Myhre, G., Samset, B. H., Schulz, M., Balkanski, Y., Bauer, S., Berntsen, T. K., Bian, H.,
771 Bellouin, N., Chin, M., Diehl, T., Easter, R. C., Feichter, J., Ghan, S. J., Hauglustaine, D.,
772 Iversen, T., Kinne, S., Kirkeväg, A., Lamarque, J. F., Lin, G., Liu, X., Lund, M. T., Luo, G.,
773 Ma, X., Van Noije, T., Penner, J. E., Rasch, P. J., Ruiz, A., Seland, Skeie, R. B., Stier, P.,
774 Takemura, T., Tsigaridis, K., Wang, P., Wang, Z., Xu, L., Yu, H., Yu, F., Yoon, J. H., Zhang,
775 K., Zhang, H. and Zhou, C.: Radiative forcing of the direct aerosol effect from AeroCom
776 Phase II simulations, Atmos. Chem. Phys., 13(4), 1853–1877, doi:10.5194/acp-13-1853-2013,
777 2013.
778 Nordmann, S., Birmili, W., Weinhold, K., Müller, K., Spindler, G. and Wiedensohler, A.:
779 Measurements of the mass absorption cross section of atmospheric soot particles using
780 Raman spectroscopy, J. Geophys. Res. Atmos., 118(21), 12075–12085,
781 doi:10.1002/2013JD020021, 2013.
782 Park, R. J., Jacob, D. J., Palmer, P. I., Clarke, A. D., Weber, R. J., Zondlo, M. A., Eisele, F.
783 L., Bandy, A. R., Thornton, D. C., Sachse, G. W. and Bond, T. C.: Export efficiency of black
784 carbon aerosol in continental outflow: Global implications, J. Geophys. Res. D Atmos.,
785 110(11), 1–7, doi:10.1029/2004JD005432, 2005.
786 Petzold, A. and Schönlinner, M.: Multi-angle absorption photometry - A new method for the
787 measurement of aerosol light absorption and atmospheric black carbon, J. Aerosol Sci., 35(4),
788 421–441, doi:10.1016/j.jaerosci.2003.09.005, 2004.
789 Petzold, A., Ogren, J. A., Fiebig, M., Laj, P., Li, S. M., Baltensperger, U., Holzer-Popp, T.,
790 Kinne, S., Pappalardo, G., Sugimoto, N., Wehrli, C., Wiedensohler, A. and Zhang, X. Y.:
791 Recommendations for reporting black carbon measurements, Atmos. Chem. Phys., 13(16),
792 8365–8379, doi:10.5194/acp-13-8365-2013, 2013.
793 Poli, A. A. and Cirillo, M. C.: On the use of the normalized mean square error in evaluating

dispersion model performance, Atmos. Environ. Part A, Gen. Top., 27(15), 2427–2434, doi:10.1016/0960-1686(93)90410-Z, 1993.

Popovicheva, O. B., Evangeliou, N., Eleftheriadis, K., Kalogridis, A. C., Movchan, V., Sitnikov, N., Eckhardt, S., Makshtas, A. and Stohl, A.: Black carbon sources constrained by observations and modeling in the Russian high Arctic, Environ. Sci. Technol., 51, 3871−3879, doi:10.1021/acs.est.6b05832, 2017.

Samset, B. H., Myhre, G., Herber, A., Kondo, Y., Li, S. M., Moteki, N., Koike, M., Oshima, N., Schwarz, J. P., Balkanski, Y., Bauer, S. E., Bellouin, N., Berntsen, T. K., Bian, H., Chin, M., Diehl, T., Easter, R. C., Ghan, S. J., Iversen, T., Kirkev??g, A., Lamarque, J. F., Lin, G., Liu, X., Penner, J. E., Schulz, M., Seland, Skeie, R. B., Stier, P., Takemura, T., Tsigaridis, K. and Zhang, K.: Modelled black carbon radiative forcing and atmospheric lifetime in AeroCom Phase II constrained by aircraft observations, Atmos. Chem. Phys., 14(22), 12465–12477, doi:10.5194/acp-14-12465-2014, 2014.

Schaap, M., Denier Van Der Gon, H. A. C., Dentener, F. J., Visschedijk, A. J. H., Van Loon, M., ten Brink, H. M., Putaud, J. P., Guillaume, B., Liousse, C. and Builtjes, P. J. H.: Anthropogenic black carbon and fine aerosol distribution over Europe, J. Geophys. Res. Atmos., 109(18), doi:10.1029/2003JD004330, 2004.

Schladitz, A., Leníček, J., Beneš, I., Kováč, M., Skorkovský, J., Soukup, A., Jandlová, J., Poulain, L., Plachá, H., Löschau, G. and Wiedensohler, A.: Air quality in the German-Czech border region: A focus on harmful fractions of PM and ultrafine particles, Atmos. Environ., 122, 236–249, doi:10.1016/j.atmosenv.2015.09.044, 2015.

Seibert, P. and Frank, A.: Source-receptor matrix calculation with a Lagrangian particle dispersion model in backward mode, Atmos. Chem. Phys., 4(1), 51–63, doi:10.5194/acp-4-51-2004, 2004.

Shevchenko, V. P., Kopeikin, V. M., Evangeliou, N., Lisitzin, A. P., Novigatsky, A. N., Pankratova, N. V, Starodymova, D. P., Stohl, A. and Thompson, R.: Atmospheric Black Carbon over the North Atlantic and the Russian Arctic Seas in Summer-Autumn Time, Химия В Интересах Устойчивого Развития, 24(4), 441–446, doi:10.15372/KhUR20160402, 2016.

Sinha, P. R., Kondo, Y., Koike, M., Ogren, J. A., Jefferson, A., Barrett, T. E., Sheesley, R. J., Ohata, S., Moteki, N., Coe, H., Liu, D., Irwin, M., Tunved, P., Quinn, P. K. and Zhao, Y.: Evaluation of ground-based black carbon measurements by filter-based photometers at two Arctic sites, J. Geophys. Res., 122(6), 3544–3572, doi:10.1002/2016JD025843, 2017.

Slinn, W. G. N.: Predictions for particle deposition to vegetative canopies, Atmos. Environ.,

16, 1785–1794, doi:10.1016/0004-6981(82)90271-2, 1982.

Stohl, A.: Characteristics of atmospheric transport into the Arctic troposphere, J. Geophys. Res. Atmos., 111(11), 1–17, doi:10.1029/2005JD006888, 2006.

Stohl, A., Hittenberger, M. and Wotawa, G.: Validation of the lagrangian particle dispersion model FLEXPART against large-scale tracer experiment data, Atmos. Environ., 32(24), 4245–4264, doi:10.1016/S1352-2310(98)00184-8, 1998.

Stohl, A., Forster, C., Frank, A., Seibert, P. and Wotawa, G.: Technical note: The Lagrangian particle dispersion model FLEXPART version 6.2, Atmos. Chem. Phys., 5(9), 2461–2474, doi:10.5194/acp-5-2461-2005, 2005.

Stohl, A., Seibert, P., Arduini, J., Eckhardt, S., Fraser, P., Greally, B. R., Maione, M., O'Doherty, S., Prinn, R. G., Reimann, S., Saito, T., Schmidbauer, N., Simmonds, P. G., Vollmer, M. K., Weiss, R. F. and Yokouchi, Y.: A new analytical inversion method for determining regional and global emissions of greenhouse gases: sensitivity studies and application to halocarbons, Atmos. Chem. Phys., 9, 1597–1620, doi:10.5194/acp-9-1597-2009, 2009.

Stohl, A., Klimont, Z., Eckhardt, S., Kupiainen, K., Shevchenko, V. P., Kopeikin, V. M. and Novigatsky, A. N.: Black carbon in the Arctic: The underestimated role of gas flaring and residential combustion emissions, Atmos. Chem. Phys., 13(17), 8833–8855, doi:10.5194/acp-13-8833-2013, 2013.

Streets, D. G., Bond, T. C., Carmichael, G. R., Fernandes, S. D., Fu, Q., He, D., Klimont, Z., Nelson, S. M., Tsai, N. Y., Wang, M. Q., Woo, J.-H. and Yarber, K. F.: An inventory of gaseous and primary aerosol emissions in Asia in the year 2000, J. Geophys. Res., 108(D21), 8809, doi:10.1029/2002JD003093, 2003.

Tarantola, A.: Inverse Problem Theory and Methods for Model Parameter Estimation, Society for Industrial and Applied Mathematics, Philadelphia, Pa., 2005.

Textor, C., Schulz, M., Guibert, S., Kinne, S., Balkanski, Y., Bauer, S., Berntsen, T., Berglen, T., Boucher, O., Chin, M., Dentener, F., Diehl, T., Easter, R., Feichter, H., Fillmore, D., Ghan, S., Ginoux, P., Gong, S., Grini, a., Hendricks, J., Horowitz, L., Huang, P., Isaksen, I., Iversen, T., Kloster, S., Koch, D., Kirkevåg, a., Kristjansson, J. E., Krol, M., Lauer, a., Lamarque, J. F., Liu, X., Montanaro, V., Myhre, G., Penner, J., Pitari, G., Lamarque, J. F., Liu, X., Montanaro, V., Myhre, G., Penner, J., Pitari, G., Reddy, S., Seland, Ø., Stier, P., Takemura, T. and Tie, X.: Analysis and quantification of the diversities of aerosol life cycles within AeroCom, Atmos. Chem. Phys., 6, 1777–1813, doi:10.5194/acpd-5-8331-2005, 2006.

Thacker, W. C.: Data assimilation with inequality constraints, Ocean Model., 16(3–4), 264–

862 276, doi:10.1016/j.ocemod.2006.11.001, 2007.
863 Thompson, R. L. and Stohl, A.: FLEXINVERT: An atmospheric Bayesian inversion
864 framework for determining surface fluxes of trace species using an optimized grid, Geosci.
865 Model Dev., 7(5), 2223–2242, doi:10.5194/gmd-7-2223-2014, 2014.
866 Thompson, R. L., Stohl, A., Zhou, L. X., Dlugokencky, E., Fukuyama, Y., Tohjima, Y., Kim,
867 S. Y., Lee, H., Nisbet, E. G., Fisher, R. E., Lowry, D., Weiss, R. F., Prinn, R. G., O'Doherty,
868 S., Young, D. and White, J. W. C.: Methane emissions in East Asia for 2000-2011 estimated
869 using an atmospheric Bayesian inversion, J. Geophys. Res. Atmos., 120(9), 4352–4369,
870 doi:10.1002/2014JD022394, 2015.
871 Thompson, R. L., Sasakawa, M., Machida, T., Aalto, T., Worthy, D., Lavric, J. V., Lund
872 Myhre, C. and Stohl, A.: Methane fluxes in the high northern latitudes for 2005-2013
873 estimated using a Bayesian atmospheric inversion, Atmos. Chem. Phys., 17, 3553–3572,
874 doi:10.5194/acp-17-3553-2017, 2017.
875 Wang, P., Wang, H., Wang, Y. Q., Zhang, X. Y., Gong, S. L., Xue, M., Zhou, C. H., Liu, H.
876 L., An, X. Q., Niu, T. and Cheng, Y. L.: Inverse modeling of black carbon emissions over
877 China using ensemble data assimilation, Atmos. Chem. Phys., 16(2), 989–1002,
878 doi:10.5194/acp-16-989-2016, 2016.
879 Wang, R., Tao, S., Balkanski, Y., Ciais, P., Boucher, O., Liu, J., Piao, S., Shen, H., Vuolo, M.
880 R., Valari, M., Chen, H., Chen, Y., Cozic, A., Huang, Y., Li, B., Li, W., Shen, G., Wang, B.
881 and Zhang, Y.: Exposure to ambient black carbon derived from a unique inventory and high-
882 resolution model., Proc. Natl. Acad. Sci. U. S. A., 111(7), 2459–63,
883 doi:10.1073/pnas.1318763111, 2014.
884 Winiger, P., Andersson, A., Eckhardt, S., Stohl, A., Semiletov, I. P., Dudarev, O. V., Charkin,
885 A., Shakhova, N., Klimont, Z., Heyes, C. and Gustafsson, Ö.: Siberian Arctic black carbon
886 sources constrained by model and observation, Proc. Natl. Acad. Sci., 114(7), E1054–E1061,
887 doi:10.1073/pnas.1613401114, 2017.
888

Atmos. Chem. Phys. Discuss., https://doi.org/10.5194/acp-2018-643
Manuscript under review for journal Atmos. Chem. Phys.
Discussion started: 23 July 2018

Atmospheric Chemistry and Physics Discussions
Open Access
EGU

889 **TABLES & LEGENDS**

890 **Table 1.** Observation sites used for the inversions (the altitude indicates the sampling height in meters above sea level).

Site ID	Organisation	Latitude	Longitude	Altitude	Year	Instrument	Description
ALT	EC/AES	82.5°N	62.5°W	205 m	2013, 2015	PSAP-3W	Alert, Nunavut, Canada
ANB	HMGU	50.6°N	13.0°E	549 m	2013	MAAP	Annaberg-Buchholz, Germany
APP	AAIRF	36.2°N	81.7°W	1110 m	2015	PSAP-3W	Appalachian SU, Boone, USA
ASP	SU	58.8°N	17.4°E	20 m	2013	PSAP	Asprveten, Västerås, Sweden
BAR	NOAA-ESRL	71.3°N	161.6°W	9 m	2013, 2014, 2015	CLAP-3W	Barrow, Alaska, USA
BIR	NILU	58.4°N	8.2°E	219 m	2014, 2015	PSAP-3W	Birkenes, Norway
BON	NOAA-ESRL	40.0°N	88.4°W	213	2015	CLAP-3W	Bondville, USA
BOS	TROPOS	53.0°N	7.9°E	53 m	2013, 2014	MAAP-5012	Bösel, Germany
CAB	ACTRIS, GAW	52.0°N	4.9°E	61 m	2013, 2014, 2015	Thermo-5012	Cabauw Zijdeweg, Netherlands
COL	NOAA-ESRL	40.4°N	106.7°W	3220 m	2015	PSAP-3W	Steamboat Springs, Colorado, USA
ETL	EC/AES	54.4°N	105.0°W	502 m	2013, 2015	PSAP-1W	East Trout Lake, Canada
GOS	NOAA	33.3°N	126.2°E	72 m	2014, 2015	CLAP-3W	Gosan, South Korea
HYY	UH, DPS	61.6°N	24.2°E	181 m	2013, 2015	Thermo-5012	Hyytiälä, Finland
KPU	HMS, ACUV	47.0°N	19.6°E	125 m	2013, 2014, 2015	CLAP-3W	K-puszta, Hungary
LEI	TROPOS	51.3°N	12.3°E	122 m	2013, 2014, 2015	MAAP-5012	Leipzig, Germany
MEL	TROPOS	51.5°N	12.9°E	86 m	2013, 2014, 2015	MAAP-5012	Melpitz, Torgau, Germany
MOU	ACTRIS, GAW	42.2°N	23.6°E	2971 m	2014, 2015	CLAP-3W	BEO Moussala, Bulgaria
MOV	-	38.1°N	8.8°W	43 m	2015	RFPS-1287	Monte Velho, Portugal
NEP	CNR	28.0°N	86.8°E	5079 m	2015	MAAP01	Nepal Climate Observatory
PAL	FMI	68.0°N	24.2°E	560 m	2013, 2014, 2015	Thermo-5012	Pallas, Sodankylä, Finland
SGP	NOAA-ESRL	36.6°N	97.5°W	318 m	2015	PSAP-3W	South Great Planes, USA
SUM	PF	72.6°N	38.5°W	3211 m	2013, 2014, 2015	CLAP-3W	Summit, Greenland
TIK	NOAA, MeteoRF	71.6°N	128.9°E	30 m	2013, 2014, 2015	Magee AE31	Tiksi, Russian Federation
TRI	NOAA-ESRL	41.1°N	124.2°W	117 m	2015	PSAP-3W	Trinidad Head, Canada
ULM	ACTRIS, GAW	50.7°N	14.8°E	161 m	2013	MAAP-CHMI	Ústí n.L.-mesto, Czechia
WHI	EC/AES	50.0°N	122.9°W	2182 m	2013, 2015	PSAP-1W	Whisper, British Columbia, Canada
WLD	GAW-WDCA	52.8°N	10.8°E	78 m	2015	MAAP-5012	Waldhof, Germany
ZEP	NCSRD	78.9°N	11.9°E	474 m	2013, 2014, 2015	Magee AE31	Zeppelin, Ny Ålesund, Norway

Atmos. Chem. Phys. Discuss., https://doi.org/10.5194/acp-2018-643
Manuscript under review for journal Atmos. Chem. Phys.
Discussion started: 23 July 2018

Table 2. Different scavenging parameters of below–cloud and in–cloud scavenging used in the ensemble model simulations for BC. A and B are rain and snow collection efficiencies for below-cloud scavenging, Ai is the cloud condensation nuclei efficiency and Bi the ice nuclei efficiency that are used in in-cloud scavenging following Grythe et al. (2017).

	A	B	A_i	B_i
BC1	1.0	1.0	0.90	0.10
BC2	1.0	1.0	0.90	0.45
BC3	1.0	1.0	0.45	0.20
BC4	1.0	0.5	0.45	0.20
BC5	0.5	0.5	0.45	0.20
BC6	1.0	0.2	0.90	0.20
BC7	1.0	1.0	0.20	0.20
BC8	2.0	1.0	0.45	0.10
BC9	0.2	0.2	0.90	0.90
BC10	1.0	1.0	0.90	0.20
BC11	2.0	1.0	0.45	0.45
BC12	1.0	1.0	0.45	0.00

Atmos. Chem. Phys. Discuss., https://doi.org/10.5194/acp-2018-643
Manuscript under review for journal Atmos. Chem. Phys.
Discussion started: 23 July 2018

900 **Table 3.** Annual prior and posterior emissions of BC for 2013, 2014 and 2015 (inversion using best representative species and best prior
901 inventory). Four different optimized emission estimates are given corresponding to use of different prior dataset.

kilotons per year	N. America	N. Europe	N. Siberia	Nenets-Komi	Khanty-Mansiysk
2013					
ACCMIPv5 (prior)	116	241	127	0.6	1.8
EDGAR_HTAPv2.2 (prior)	117	163	108	0.3	0.6
MACCity (prior)	117	244	129	0.6	1.9
ECLIPSEv5 (prior)	148	352	187	26	25
Posterior (ECLIPSEv5)	149±45	152±46	230±66	17±5	32±8
2014					
ACCMIPv5 (prior)	130	253	178	0.5	1.9
EDGAR_HTAPv2.2 (prior)	131	175	159	0.3	0.7
MACCity (prior)	131	256	179	0.5	1.8
ECLIPSEv5 (prior)	162	364	238	25	26
Posterior (ECLIPSEv5)	193±61	124±44	291±73	15±5	28±8
2015					
ACCMIPv5 (prior)	149	250	155	0.5	1.8
EDGAR_HTAPv2.2 (prior)	150	172	136	0.3	0.6
MACCity (prior)	150	252	156	0.6	1.8
ECLIPSEv5 (prior)	182	381	222	25	25
Posterior (ECLIPSEv5)	181±55	238±66	130±52	14±5	37±8
3-year average emissions	**174±58**	**170±59**	**217±69**	**15±5**	**32±8**

902

Atmos. Chem. Phys. Discuss., https://doi.org/10.5194/acp-2018-643
Manuscript under review for journal Atmos. Chem. Phys.
Discussion started: 23 July 2018

Atmospheric Chemistry and Physics Discussions

904 **FIGURES & LEGENDS**

905

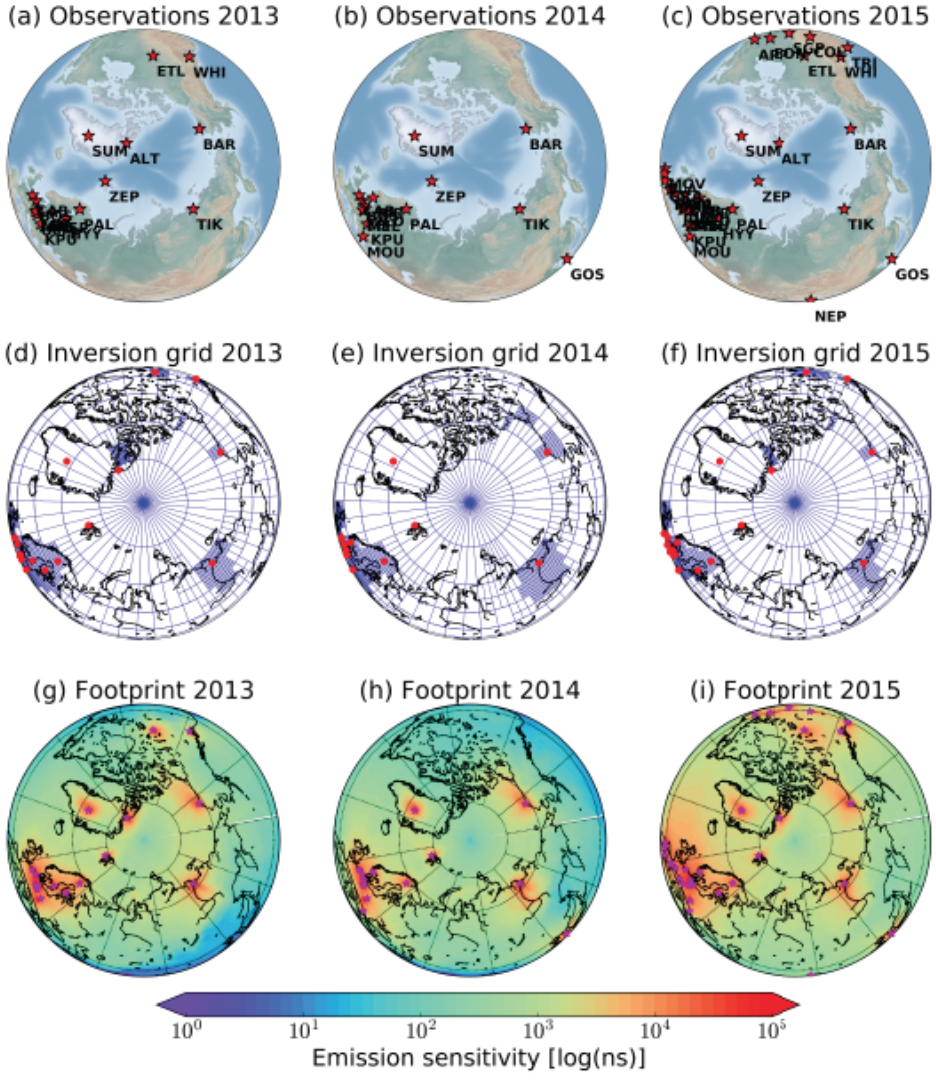

906

907 **Figure 1.** Observation network used for the present inversion (a, b and c), and variable-
908 resolution grid used for the inversion (d, e, and f) also showing the location of the observation
909 sites (red stars) for 2013–2015 period. Sensitivity to the surface emissions (i.e., the footprint
910 emission sensitivity or equivalently source-receptor relationship) integrated over all
911 observation sites and all time steps (g, h and i) for the years 2013, 2014 and 2015 (units of
912 log(ns)).

Atmos. Chem. Phys. Discuss., https://doi.org/10.5194/acp-2018-643
Manuscript under review for journal Atmos. Chem. Phys.
Discussion started: 23 July 2018

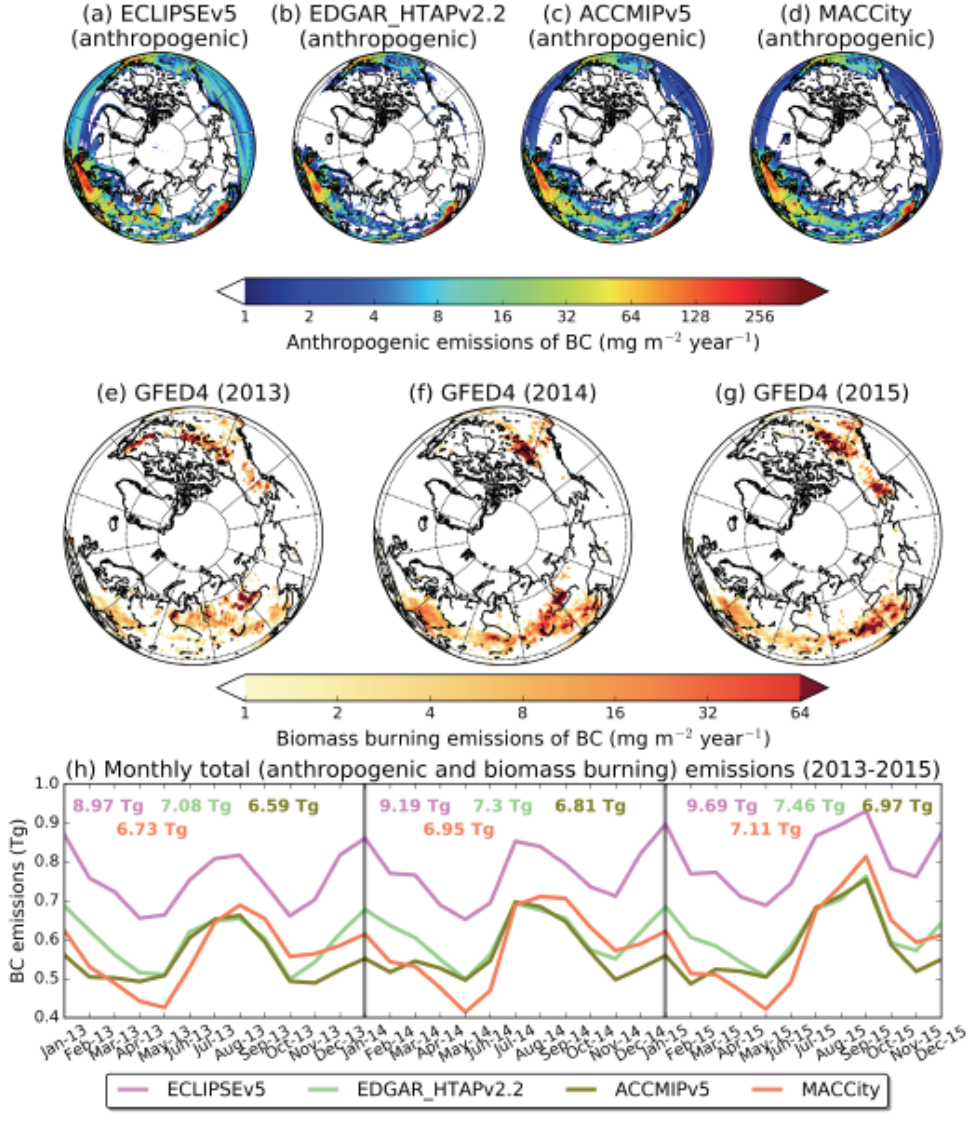

Figure 2. (a–d) Anthropogenic emissions of BC in the inversion domain (>50°N) from ECLIPSEv5, EDGAR_HTAPv2.2, ACCMIPv5 and MACCity (anthropogenic emissions are assumed to be constant throughout every year). (e–g) Biomass burning emissions from GFED4 for 2013, 2014 and 2015 (Giglio et al., 2013). (h) Monthly total (anthropogenic and biomass burning) emissions of BC north of 50°N from 2013 to 2015 from the four prior inventories used for the inversion. Coloured numbers correspond to total annual BC from each emission inventory.

Atmos. Chem. Phys. Discuss., https://doi.org/10.5194/acp-2018-643
Manuscript under review for journal Atmos. Chem. Phys.
Discussion started: 23 July 2018

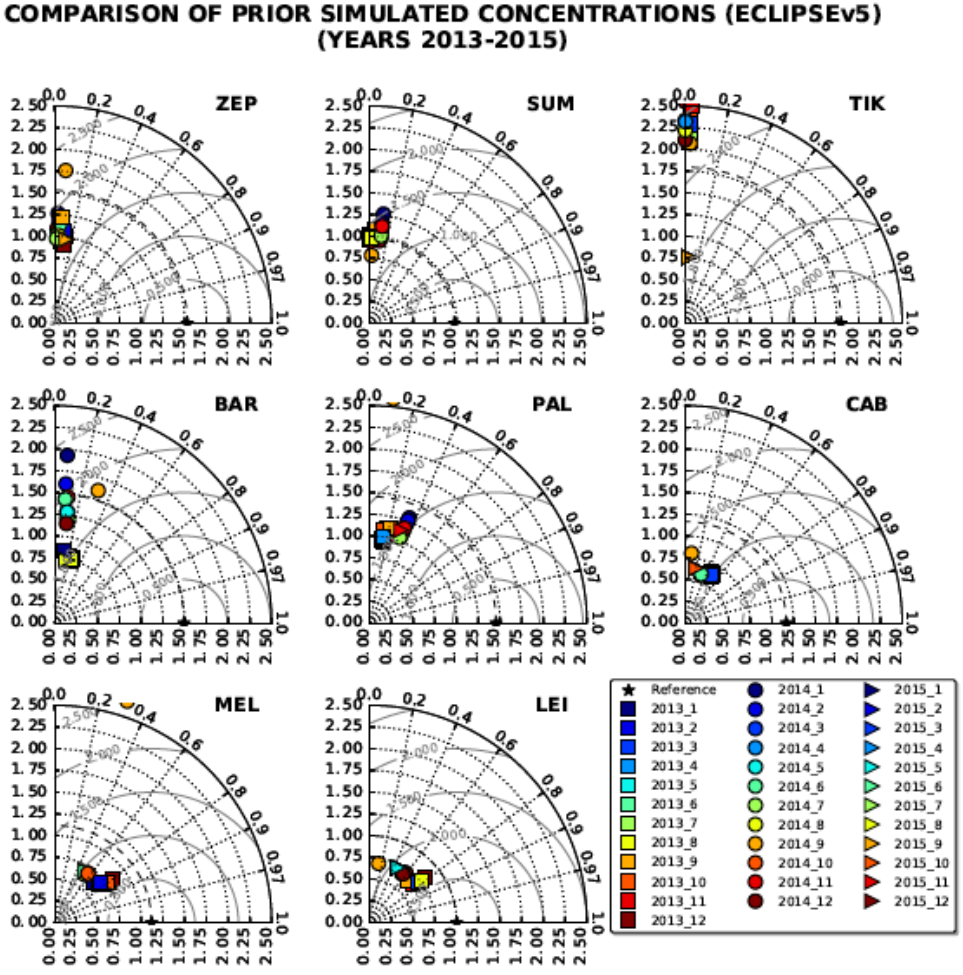

Figure 3. Taylor diagrams for the comparison of the prior (ECLIPSEv5) simulated concentrations with observations for all years (2013 – 2015) for 12 BC species with different scavenging coefficients (**Table 2**). The radius indicates standard deviations normalised against the mean concentration (NSD); the azimuthal angle the Pearson correlation coefficient, while the normalised (against observation) root mean square error (nRMSE) in the simulated concentrations is proportional to the distance from the point on the x-axis identified as "reference" (grey contours).

Atmos. Chem. Phys. Discuss., https://doi.org/10.5194/acp-2018-643
Manuscript under review for journal Atmos. Chem. Phys.
Discussion started: 23 July 2018

Atmospheric Chemistry and Physics Discussions

931

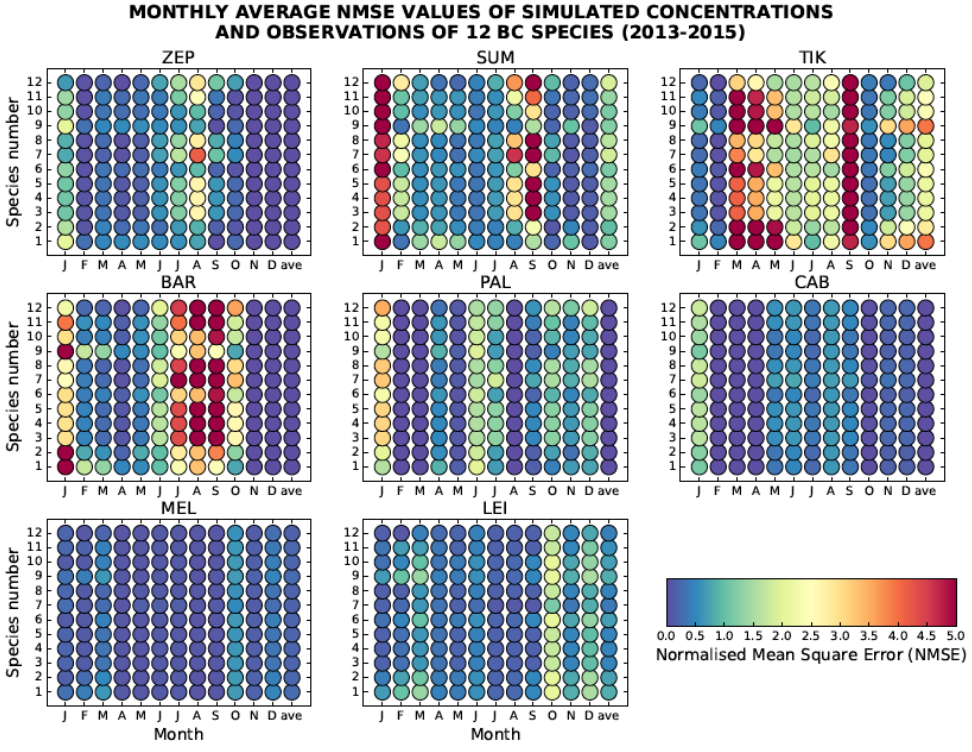

932

933 **Figure 4.** Monthly average NMSE values due to use of 12 different BC species defined in
934 **Table 2** for the eight stations with complete data in the period 2013–2015. The annual mean
935 is denoted as "ave").

936

Atmos. Chem. Phys. Discuss., https://doi.org/10.5194/acp-2018-643
Manuscript under review for journal Atmos. Chem. Phys.
Discussion started: 23 July 2018

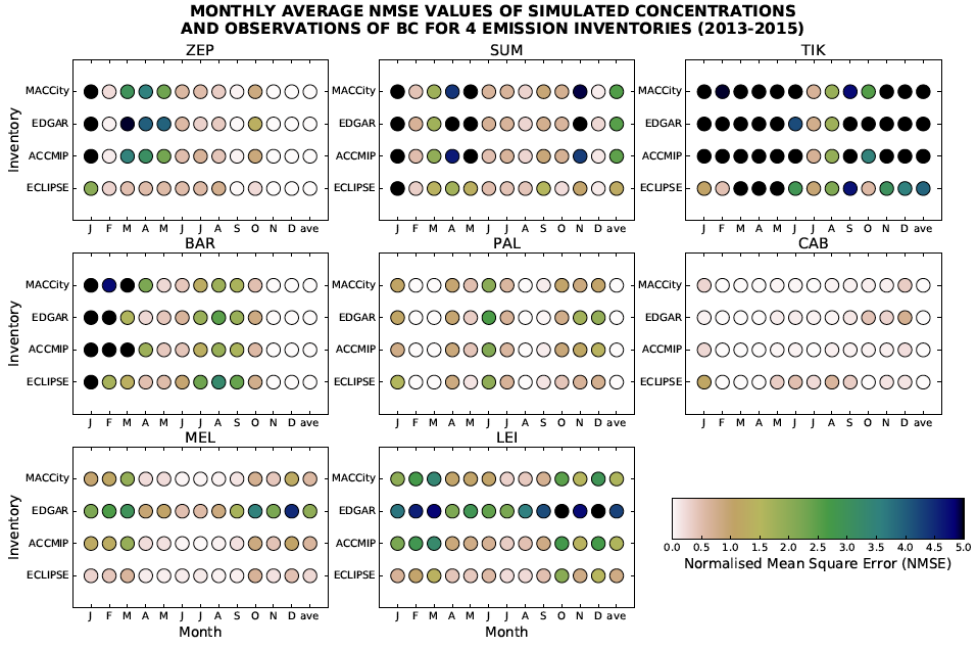

Figure 5. Monthly average NMSE values due to use of different emission inventories (ECLIPSEv5, ACCMIPv5, EDGAR_HTAPv2.2, MACCity) for the eight stations with complete data in the period 2013–2015. The annual mean is denoted as "ave").

Atmos. Chem. Phys. Discuss., https://doi.org/10.5194/acp-2018-643
Manuscript under review for journal Atmos. Chem. Phys.
Discussion started: 23 July 2018

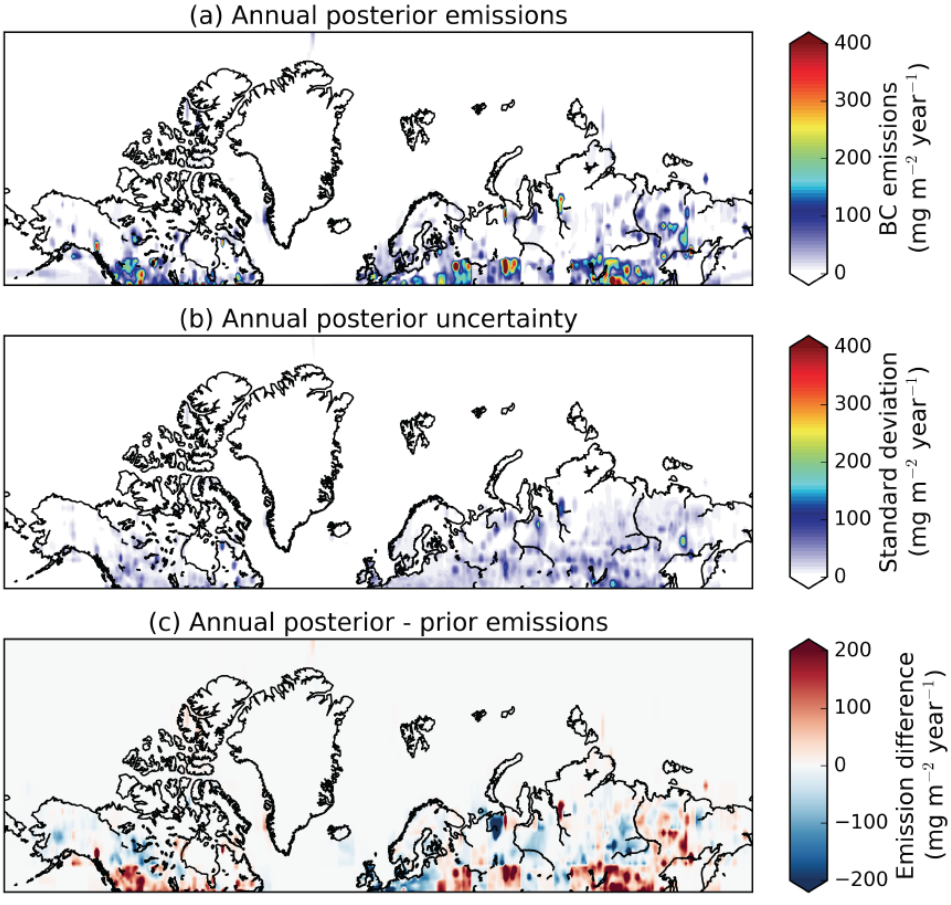

Figure 6. (a) Annual posterior emissions of BC in areas >50°N averaged for the period 2013–2015, (b) average posterior uncertainty due to scavenging and use of different prior emissions for the same period. (c) Difference between posterior and prior emissions for 2013–2015.

Atmos. Chem. Phys. Discuss., https://doi.org/10.5194/acp-2018-643
Manuscript under review for journal Atmos. Chem. Phys.
Discussion started: 23 July 2018

Atmospheric Chemistry and Physics Discussions

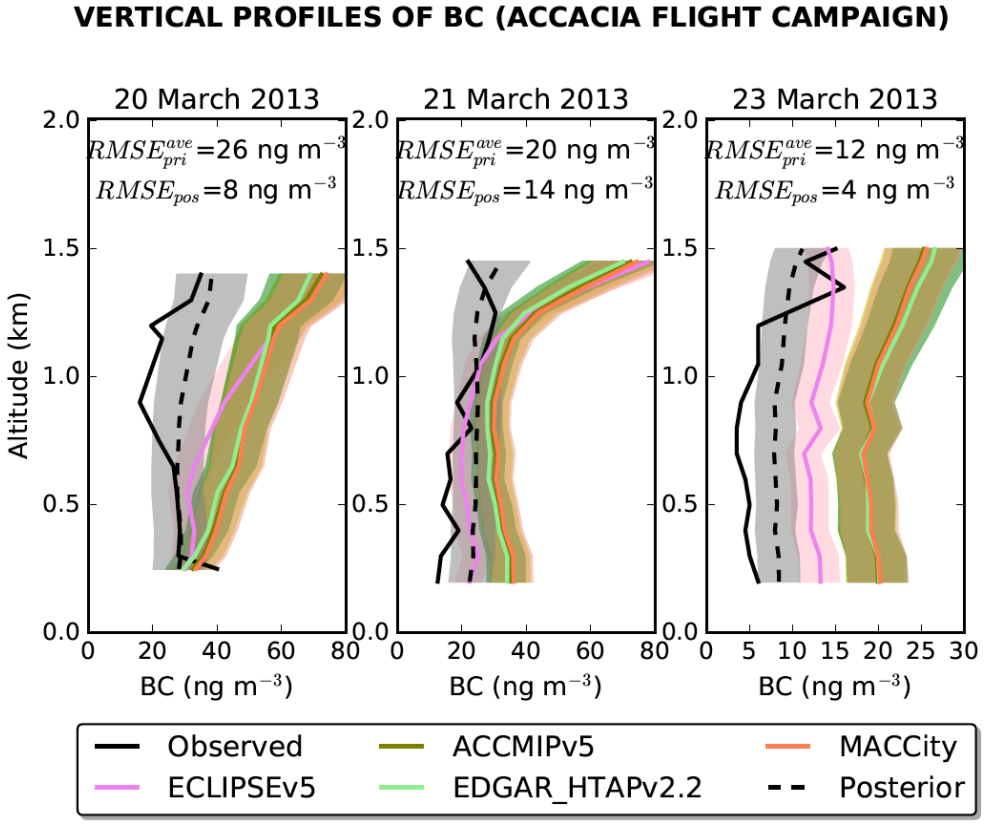

947

948 **Figure 7.** Comparison of prior (ECLIPSEv5, ACCMIPv5, EDGAR HTAPv2.2 and
949 MACCity) and posterior simulated concentrations of BC with observations from the
950 ACCACIA flight campaign near Zeppelin station, Ny-Ålesund in 2013 adopted from Sinha et
951 al. (2017). The variability of the prior concentrations (shaded area) was calculated as the
952 standard deviation of BC concentrations from the 12 species with different scavenging
953 coefficients as shown in **Table 2**. Uncertainties of the posterior concentrations are due to
954 scavenging and use of 4 different a priori datasets (section 3.4).

955

Atmos. Chem. Phys. Discuss., https://doi.org/10.5194/acp-2018-643
Manuscript under review for journal Atmos. Chem. Phys.
Discussion started: 23 July 2018

Atmospheric Chemistry and Physics Discussions

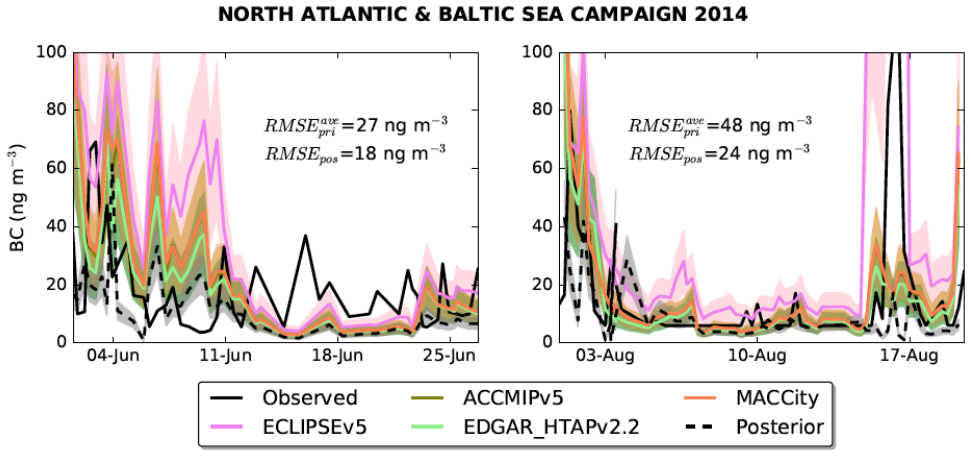

956

957 **Figure 8.** Comparison of prior (ECLIPSEv5, ACCMIPv5, EDGAR HTAPv2.2 and
958 MACCity) and posterior simulated concentrations of BC with observations from a ship
959 campaign in North Atlantic and Baltic Seas in 2014 adopted from Shevchenko et al. (2016).
960 The variability of the prior concentrations (shaded area) was calculated as the standard
961 deviation of BC concentrations from the 12 species with different scavenging coefficients as
962 shown in **Table 2**. Uncertainties of the posterior concentrations are due to scavenging and use
963 of 4 different a priori datasets (section 3.4).

964

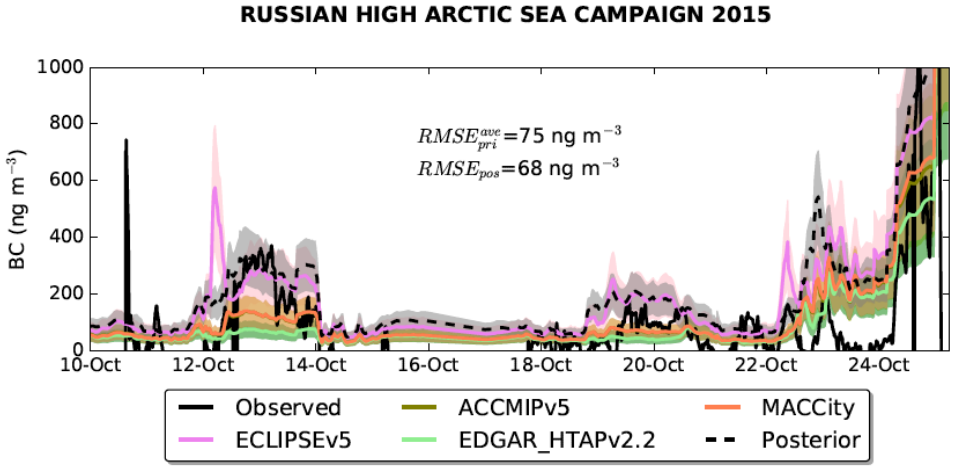

965

966 **Figure 9.** Comparison of prior (ECLIPSEv5, ACCMIPv5, EDGAR HTAPv2.2 and
967 MACCity) and posterior simulated concentrations of BC (2015) with observations from a
968 ship campaign in the Russian Arctic in 2015 adopted from Popovicheva et al. (2017). The
969 variability of the prior concentrations (shaded area) was calculated as the standard deviation
970 of BC concentrations from the 12 species with different scavenging coefficients as shown in
971 **Table 2**. Uncertainties of the posterior concentrations are due to scavenging and use of 4
972 different a priori datasets (section 3.4).

973

Atmos. Chem. Phys. Discuss., https://doi.org/10.5194/acp-2018-643
Manuscript under review for journal Atmos. Chem. Phys.
Discussion started: 23 July 2018

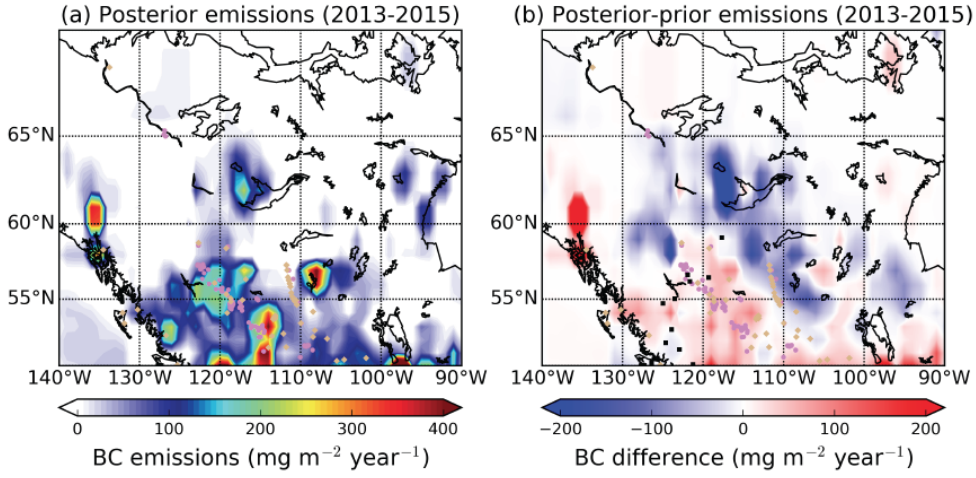

974

975 **Figure 10.** (a) Optimised emissions of BC in North America (Western Canada) averaged over
976 the 2013–2015 period. (b) Difference between a posteriori and a priori emissions of BC
977 (ECLIPSEv5 was used as the prior). Magenta points on the map denote the gas flaring
978 industries from the Global Gas Flaring Reduction Partnership (GGFR)
979 (http://www.worldbank.org/en/programs/gasflaringreduction), grey points show the power
980 industries that operate using fossil fuels and oil and gas production and oil refining industries
981 adopted from Industry About (https://www.industryabout.com/canada-industrial-map), while
982 black rectangles show active fires from MODIS.

983

Atmos. Chem. Phys. Discuss., https://doi.org/10.5194/acp-2018-643
Manuscript under review for journal Atmos. Chem. Phys.
Discussion started: 23 July 2018

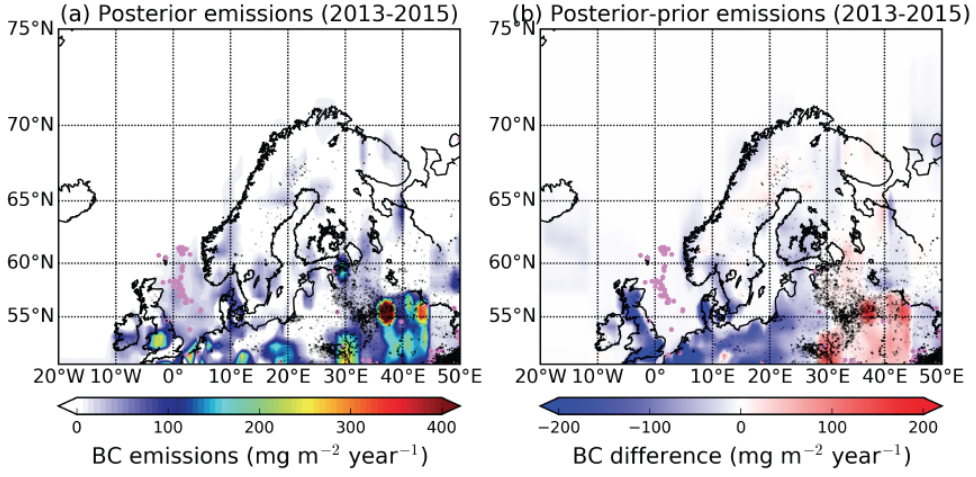

Figure 11. (a) Optimised emissions of BC in Northern Europe averaged over the 2013–2015 period. (b) Difference between a posteriori and a priori emissions of BC (ECLIPSEv5 was used as the prior). Magenta points on the map indicate the gas flaring industries from the Global Gas Flaring Reduction Partnership (GGFR) (http://www.worldbank.org/en/programs/gasflaringreduction), while black rectangles show the vegetation fires adopted from Hao et al. (2016).

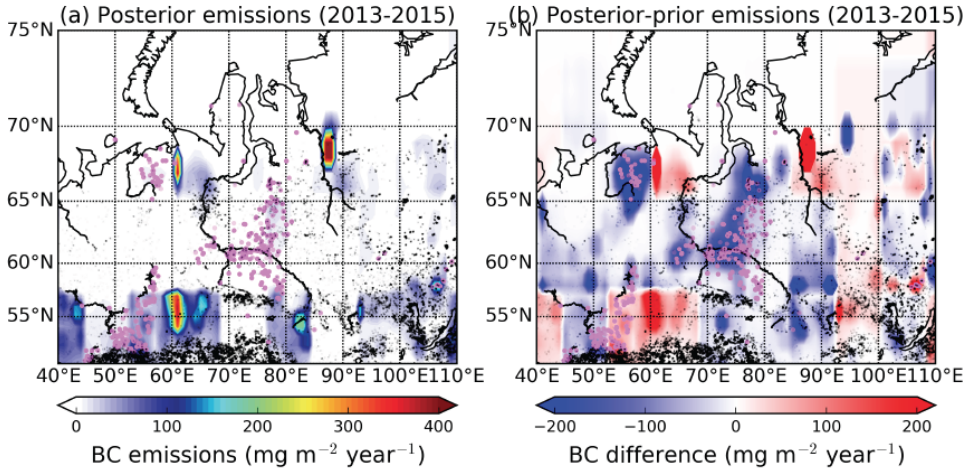

992

993 **Figure 12.** (a) Optimised emissions of BC in Western Siberia averaged for the 2013–2015
994 period. (b) Difference between a posteriori and a priori emissions of BC (ECLIPSEv5 was
995 used as the prior). Magenta points on the map indicate the gas flaring industries from the
996 Global Gas Flaring Reduction Partnership (GGFR)
997 (http://www.worldbank.org/en/programs/gasflaringreduction), while black rectangles show
998 the vegetation fires adopted from Hao et al. (2016).

999

Atmos. Chem. Phys. Discuss., https://doi.org/10.5194/acp-2018-643
Manuscript under review for journal Atmos. Chem. Phys.
Discussion started: 23 July 2018

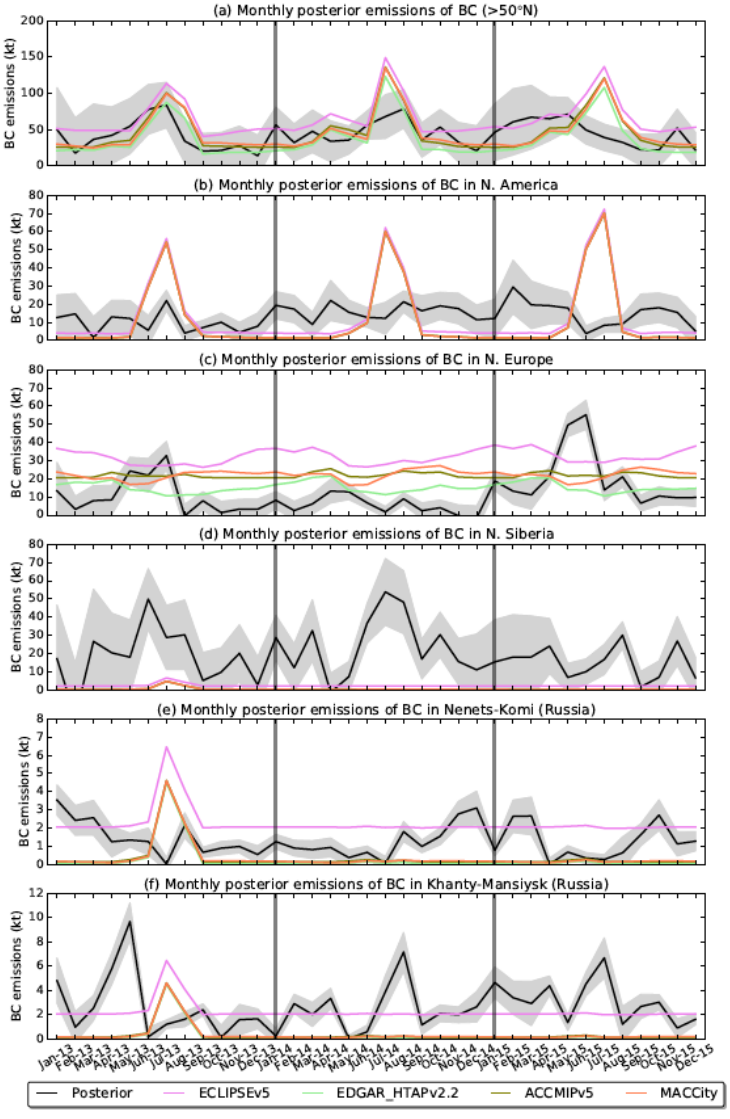

Figure 13. Monthly posterior emissions of BC shown for all regions located (a) >50°N, (b) in North America (>50°N), (c) North Europe (>50°N), (d) North Siberia (>50°N), (e) Nenets-Komi oblast (>50°N, Russia) and (f) Khanty-Mansiysk oblast (>50°N, Russia) for the 2013–2015 period. Monthly prior emissions of BC from ECLIPSEv5, EDGAR_HTAPv2.2, ACCMIPv5 and MACCity emissions inventories are also shown for the same regions and time period. The uncertainty of the posterior emissions of BC stems from the use of different scavenging coefficients and different prior emission datasets (see section 3.3).